*minerals*

MDPI

*Article*

# Uranium Mineralization in the MacInnis Lake Area, Nonacho Basin, Northwest Territories: Potential Linkages to Metasomatic Iron Alkali-Calcic Systems

**Kerstin Landry [1], Erin Adlakha [1,*], Andree Roy-Garand [1], Anna Terekhova [1], Jacob Hanley [1], Hendrik Falck [2] and Edith Martel [2]**

[1] Department of Geology, Saint Mary's University, 923 Robie St., Halifax, NS B3H 3C3, Canada
[2] Northwest Territories Geological Survey, 4601-B 52 Avenue, Yellowknife, NT X1A 1K3, Canada
* Correspondence: erin.adlakha@smu.ca

**Abstract:** The intracratonic Paleoproterozoic Nonacho Basin, deposited on the western margin of the Rae craton, contains historic polymetallic (i.e., U, Cu, Fe, Pb, Zn, Ag) occurrences spatially associated with its unconformable contact with underlying crystalline basement rocks and regionally occurring faults. This study presents the paragenesis, mineral chemistry and geochemistry of uranium mineralized rocks and minerals of the MacInnis Lake sub-basin of the Nonacho Basin, to evaluate the style and relative timing of uranium mineralization. Mineralization is restricted to regionally occurring deformation zones, and post-dates widely spread and pervasive albitization and more local Ba-rich K-feldspar alteration of host rocks. Uranium mineralized rocks show elevated concentration of Cu, Ag and Au relative to variably altered host rocks. Microscopic and compositionally heterogeneous altered uraninite occurs (i) as overgrowths on partially dissolved Cu-sulphides with magnetite in chlorite ± quartz, calcite veins, and (ii) with minor uranophane in hematite-sericite-chlorite ± quartz breccia and stockwork. Both uraninite types are Th poor (<0.09 wt.% $ThO_2$) and variably rich in $SO_4$ (up to 2.26 wt.%), suggesting a low-temperature hydrothermal origin in a relatively oxidized environment. Rare-earth element (+Y) concentrations in type-i uraninite are high, up to 9.5 wt.% $\Sigma(REE+Y)_2O_3$ with $Ce_N/Y_N$ values > 1, similar to REE compositions of uraninite in metasomatic iron and alkali-calcic systems (MIAC), including low-temperature hematite-type IOCG-deposits (e.g., Olympic Dam, Gawler Craton, Australia) and albitite-hosted uranium deposits (e.g., Southern Breccia, Great Bear Magmatic Zone, Canada, and Gunnar Deposit, Beaverlodge District, Canada). Both uraninite types are variably rich in Ba (up to 3 wt.% BaO), a geochemical marker for MIAC systems, provided by the dissolution of earlier secondary Ba-rich K-feldspar. Chemical U-Th-Pb dating yields minimum ages of 1757 to 1739 ± 70 Ma for type-ii uraninite-uranophane, consistent with strike-slip movement along regional structures of the basin. We suggest that MacInnis Lake uranium occurrences formed from oxidized hydrothermal fluids along previously altered (albitized, potassically altered) regional-scale faults. Uranium minerals precipitated on earlier Fe-rich sulfides (chalcopyrite, bornite), which acted as a redox trap for mineralization, in low-temperature (~310–330 °C, based on Al-in-chlorite thermometry) breccias and stockwork zones, late in a metasomatic iron and alkali-calcic alteration system.

**Keywords:** metasomatism; albitization; rare earth elements; Rae craton; IOCG



**Citation:** Landry, K.; Adlakha, E.; Roy-Garand, A.; Terekhova, A.; Hanley, J.; Falck, H.; Martel, E. Uranium Mineralization in the MacInnis Lake Area, Nonacho Basin, Northwest Territories: Potential Linkages to Metasomatic Iron Alkali-Calcic Systems. *Minerals* **2022**, *12*, 1609. https://doi.org/10.3390/min12121609

Academic Editor: David Quirt

Received: 9 November 2022
Accepted: 11 December 2022
Published: 14 December 2022



## 1. Introduction

The fault-bound, Paleoproterozoic, siliciclastic Nonacho Basin in southeastern Northwest Territories (Figure 1) is the host of over 60 uranium occurrences, which have been the subject of mineral exploration since the 1950s [1–17]. Despite over 70 years of exploration, and the proximity to the Athabasca and Thelon basins that host world-class unconformity-type uranium deposits, the uranium occurrences of the Nonacho Basin are

not well characterized and have yet to be formally classified (e.g., unconformity-related deposits, sandstone-hosted deposits, hematite breccia complex deposits, metasomatic deposits, vein-type deposits). The majority of work has been concentrated on the numerous uranium occurrences in the MacInnis Lake area, a roughly 200 $km^2$ northeast-trending sub-basin in the larger Nonacho Basin (Figure 1). Gandhi and Prasad [15] and Kuronuma [17] described the prospects primarily based on field observations and preliminary whole-rock geochemical and isotopic data. The authors suggest that mineralization is predominantly pitchblende, commonly associated with secondary uranium minerals (e.g., uranophane) and chlorite that occur in stockwork-like veins and along fractures within basement rocks, Nonacho sediments and late gabbroic intrusions, as well as disseminations in arkosic sedimentary rocks. They suggest the former occurrences are vein-type deposits that formed during deformation, which was agreed upon by Jefferson [18].

The mineralogy of uranium is strongly influenced by oxidation conditions, as well as the composition of the environment [19]. Uraninite ($UO_2$) is the main uranium ore mineral; however, it can deviate far from ideal composition, recording its formation environment. For example, high temperature (>350 °C) magmatic and metasomatic uraninite can incorporate high concentrations of $Th^{4+}$ (reflecting the solid solution series uraninite-thorite), as well as trivalent rare earth elements (REE) and Y, whereas low temperature (<350 °C), hydrothermal uraninite tends to be poor in these elements due to their lack of mobility in low temperature fluids [20,21]. Uraninite is also strongly susceptible to alteration by later oxidizing fluids [22,23]. The production of radiogenic $Pb^{4+}$ causes auto-oxidation of $U^{4+}$ to $U^{6+}$ through the reduction of $Pb^{4+}$ to $Pb^{2+}$. However, $Pb^{2+}$ does not fit in the crystal structure of uraninite, tends to migrate out of the uraninite, and subsequent alteration and substitution of $Pb^{2+}$ occur with a variety of smaller cations (e.g., Ca, Fe, Si) [19,22]. Uraninite is commonly altered and remobilized to secondary uranyl hydroxysilicate minerals like uranophane; although, uranophane can precipitate directly from oxidized fluids [19].

The purpose of this study is to describe and characterize the uranium mineralization of the MacInnis Lake sub-basin that hosts at least twenty-one uranium occurrences. Six occurrences, hosted in basement or sedimentary rocks of the Nonacho Basin (Kult-82, Island, Pyramid, Cole, Welch and Dussault), were selected for detailed petrography, whole-rock geochemical analyses and mineral chemistry in effort to determine the paragenetic relationship and the origin for hydrothermal uranium occurrences in the MacInnis Lake area, which may be an analogue for other uranium occurrences in the Nonacho Basin and Paleoproterozoic basins with similar metallogeny.

## 2. Geological Background

### *2.1. Regional Geology*

The Nonacho Basin overlies the Rae craton of the western Churchill Province. The western Churchill Province is composed of two Meso-Neoarchean cratons; the Rae and the Hearne. The Rae craton is a crustal block, which extends > 1000 km from northern Canada into Greenland [24]. It is bounded by 2.0 to 1.9 Ga orogenic and tectonic belts (Figure 1) that formed during the amalgamation of Laurentia, the ancestral North American core [25], and the supercontinent Nuna [26]. The 2.0–1.9 Ga Taltson and Thelon suture zones border the western Rae (Figure 1) and formed during the collision of the Slave craton and Buffalo Head terrane with the Rae craton [25,27]. This collision caused lateral escape at 1.93 to 1.94 Ga and sinistral strike-slip faulting that bounds the Nonacho Basin [28–30].

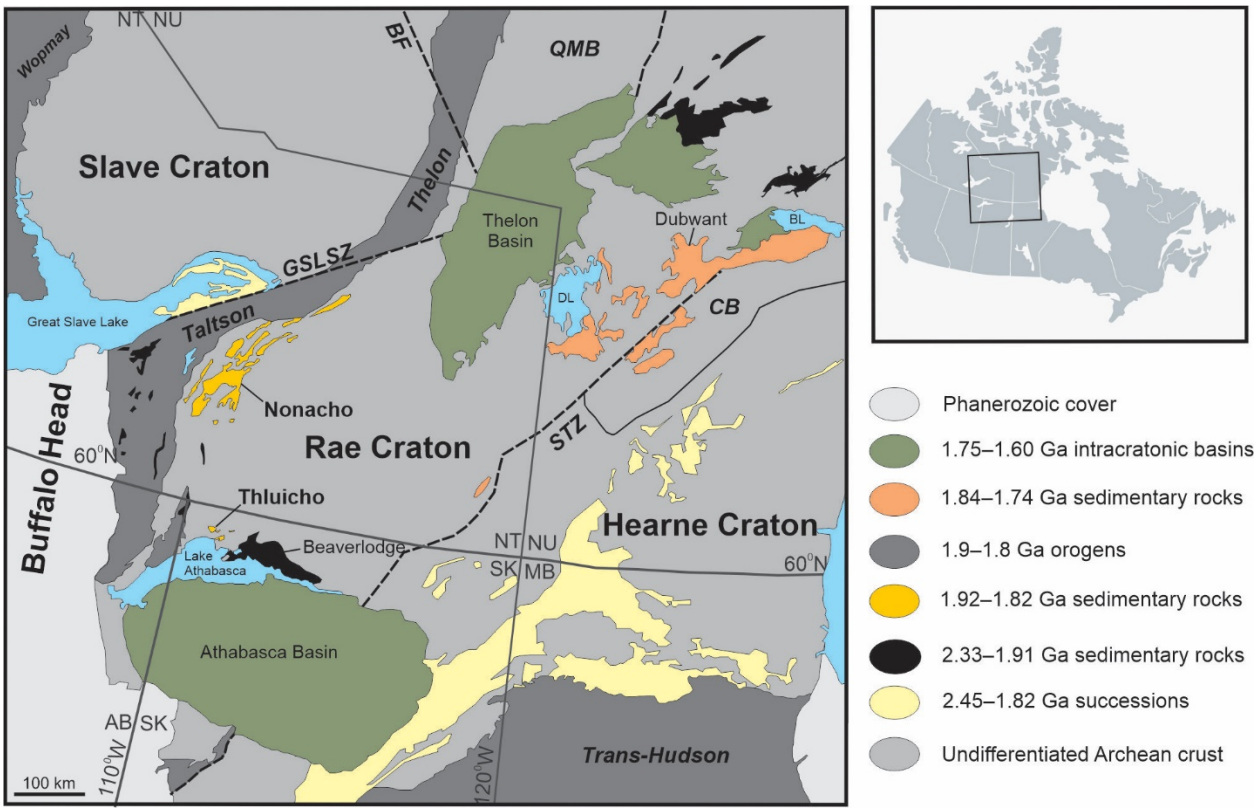


**Figure 1.** Generalized regional map showing the location of the Nonacho Basin relative to major lithotectonic domains. Abbreviations: BF—Bathurst Fault; BL—Baker Lake; CB—Chesterfield Block; DL—Dubwant Lake; GSLSZ—Great Slave Lake Shear Zone; STZ—Snowbird Tectonic Zone; QMB; Queen Maud block. Canadian Provinces and Territories: AB—Alberta; MB—Manitoba; NT—Northwest Territories; NU—Nunavut; SK—Saskatchewan. Dashed lines mark major structures and faults. Figure modified after [29,31].

### *2.2. Local Geology*

The Nonacho Basin is a northeast-striking Paleoproterozoic basin, measuring 200 × 60 km in size [32], that lies southeast of Great Slave Lake (Figure 1). It formed in response to a sinistral strike-slip faulting regime, comprising several rhomb, wedge, and rectangular sub-basins (e.g., MacInnis; Salkeld; Sparks; Taltson; Naskethey; Figure 2a; [28,33]). The Archean basement rocks consist of variably metamorphosed gneisses, granitoids, metasedimentary and metavolcanic rocks [28,33], unconformably overlain by the Nonacho Group sedimentary sequence.

The Nonacho Group is a sedimentary siliciclastic succession deposited between 1.91 and 1.83 Ga [28,33]. Reconnaissance mapping of the Nonacho Basin dates back to Henderson [34], with a comprehensive effort to reconstruct the stratigraphy and structural evolution of the basin performed by Aspler [33] and reappraised by Ielpi [32]. The stratigraphic sequence is divided into six formations and three fining, or coarsening upward sequences, which are subdivided into two groups based on differences in their clast compositions: the lower and upper Nonacho Groups (Figure S1; [10]). The lower Nonacho Group consists of the Hjalmar (conglomerate, sandstone), Tronka Chua (sandstone), Chief Nataway (sandstone, shale) and Newshethdezza (sandstone) formations, and lithic clasts are dominantly sourced from the local Archean basement rocks (granitoid, orthogneiss and amphibolite; [10]). The upper Nonacho Group consists of the Thekulthili (conglomerate, sandstone) and Taltson (sandstone, shale) formations, which locally and unconformably overly both the Tronka Chua Formation and the crystalline basement. These formations contain a more diverse clast assemblage, including intrabasinal sandstones and conglomer-

ates, vein quartz, granitoid rocks, quartz arenite and felsic-mafic volcanic rocks. Aspler [33] interpreted the Nonacho Group formations to record scree-slope, alluvial fan, fluvial, and lacustrine depositional environments of a foreland molasse, which formed during the Trans-Hudson Orogeny. However, reappraisal by Ielpi et al. [32] suggests alluvial (fluvial dominated), shoal-water deltaic, nearshore marine and deep-water-marine depositional settings. Along with a variety of sedimentological indicators (e.g., wave- and bimodal-ripple hummocky cross, and Flaser stratifications) documented by Ielpi et al. [32], this rules out an entirely terrestrial origin for Nonacho Group sedimentation.

Detrital zircon geochronology by Van Breeman et al. [30] and Neil et al. [31] indicate an apparent change in provenance from the lower to upper Nonacho Group, where there is an increase in detritus up-stratigraphy derived from the 2.0 to 1.9 Ga Taltson-Thelon orogenies. This constrains the maximum depositional age of the upper Nonacho Group to 1907 $\pm$ 15 Ma [32]. The Sparrow Dike Swarm cross-cuts the Nonacho Group sediments, except for the lowermost Hjalmar Formation, thus constraining the minimum age of deposition to 1827 $\pm$ 4 Ma [35].

### *2.3. Geology and Mineral Occurrences at MacInnis Lake*

The MacInnis Lake sub-basin is located along the western margin of the Nonacho Basin and bound by a series of north-northeast trending faults (Figure 2a) The MacInnis Lake area is host to numerous historic uranium and base-metal occurrences (Figure 2b).

The lithology of the MacInnis Lake area includes crystalline basement granitoids unconformably overlain by the lowermost Hjalmar granite-pebble conglomerate, and interbedded sandstones and mudstone of the Tronka Chua Formation. There is a break in stratigraphy, with an absence of the upper-most Chief Nataway and Newshethdezza Formations of the lower Nonacho Group, resulting in the Thekulthili and Taltson Formations of the upper Nonacho Group unconformably overlying the basement granitoids [7].

Unaltered gabbroic dikes and intrusive bodies cross-cut the basement and overlying Nonacho sedimentary rocks (Figure 2b). Gabbroic dikes cross-cutting the basement are up to 30 m wide, and crop out at the Island occurrence, covered in this study. In contrast, mafic dykes cross-cutting the Nonacho sediments are relatively thin.

The MacInnis Lake sub-basin is variably faulted, sheared and deformed [32]. The sub-basin is bordered along its western margin by the Taltson and Thekulthili formations (Figure 2b). Although the basement contact appears conformable, Jefferson [18] suggests that this contact is a zone of repeated shearing which has undergone a prolonged history of tectonically-driven vein-hosted uranium mineralization. Gandhi and Prasad [7] note that the Taltson and Thekulthili sediments have undergone north-northeast trending synclinal folding, as well as varying east-northeast subsidiary folds and cross-folds. The less competent units of the Taltson Formation have undergone more complex and severe drag-folding and crenulations [7]. Several steeply-dipping north to northeast trending faults were observed in the area and are locally associated with a series of quartz veins [7]. The eastern margin of the MacInnis Lake sub-basin is bordered by a high-strain zone within the Hjalmar Formation (Figure 2b). The Hjalmar Formation is interpreted to have been deposited along strike-slip faults during basin development [29], and sheared during fault reactivation [18]. Canam et al. [36] describe sinistral, trans-tensional, greenschist-facies reactivation of faults at 1.78 Ga, which flank the Nonacho basin and occurred following main basin development. Vein-hosted uranium occurrences are localized within the sheared western margin of the Hjalmar Formation and along other structurally disturbed settings of the MacInnis Lake sub-basin [18] (Figure 2b). Mineral resource information for the occurrences is lacking; however, a historical mineral resource estimate for the Dussault Prospect reports 27,000 metric tonnes averaging 0.17% U ([15], and references therein).

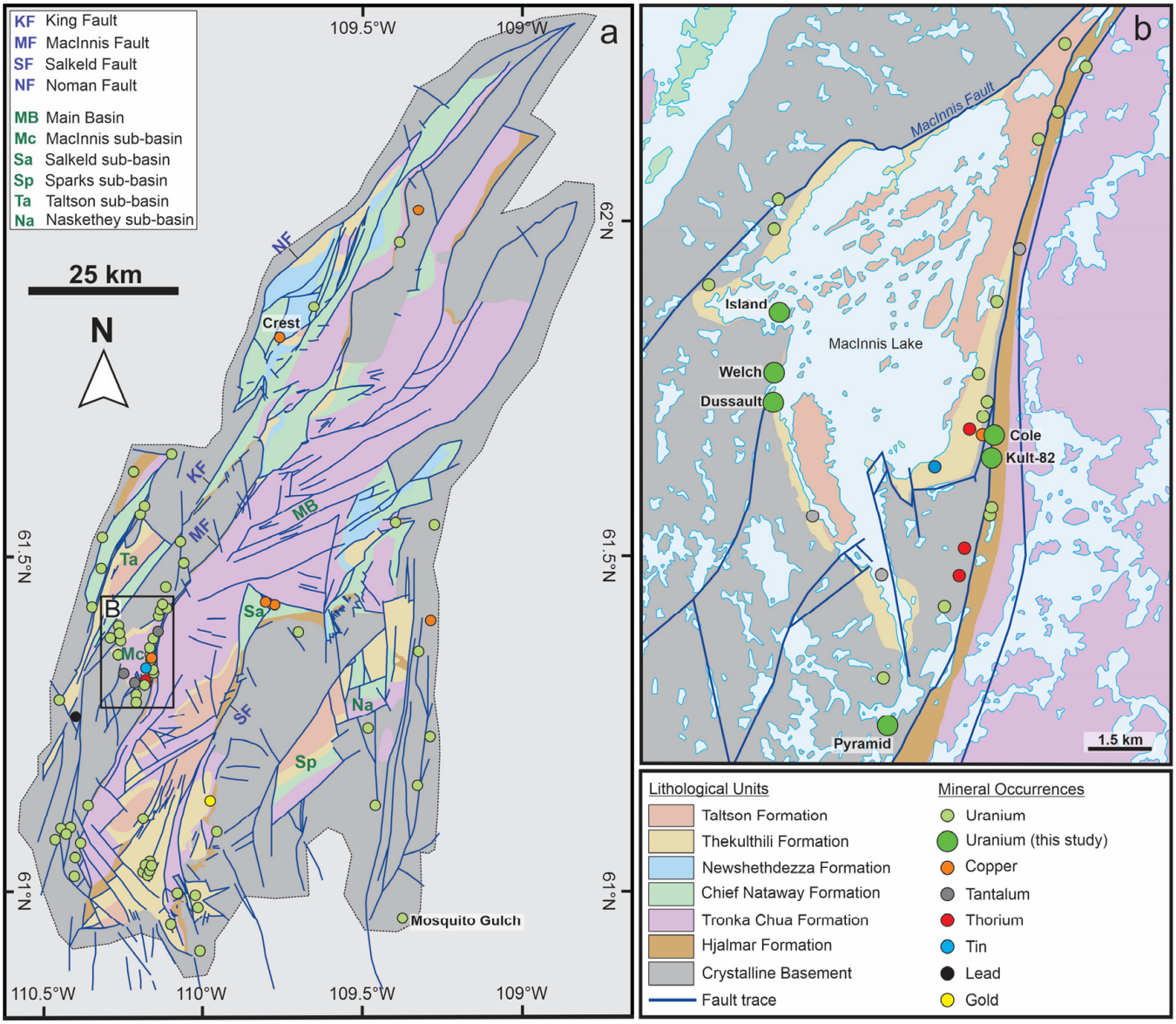


**Figure 2.** Geological sketches of the Nonacho Basin showing the location of notable uranium and base metal occurrences. (**a**) The Nonacho Basin showing major faults, lithologies, and sub-basins (labeled), with the MacInnis Lake area outlined. Modified after Aspler [33] and Ielpli et al. [32]; (**b**) Geology and mineral occurrences of the MacInnis Lake Area. Uranium occurrences investigated in this study are labelled. Modified from [7,37,38].

## 3. Materials and Methods

### *3.1. Field Work and Sampling*

Host rocks, alteration, mineralization and structures of the uranium showings were documented in the field. Representative samples with uranium minerals (detected by high radioactivity) and associated alteration in a variety of host lithologies were collected and listed in Table 1. Some archived samples were provided by the Geological Survey of Canada (GSC) in Ottawa, collected by Dr. Sunil Gandhi in 1978.

**Table 1.** Summary of representative mineralized samples and styles of uranium mineralization at the MacInnis Lake occurrences, Nonacho Basin.

| Occurrence | UTM Coordinates (Zone 12V, NAD83) | Sample | Host Lithology | U-Species | Habit, Grain Size and Texture of U Mineralization | U Associated Minerals |
|---|---|---|---|---|---|---|
| Kult-82 | 0546206, 6800134 | K82-C1, K82-C2 | Basement granitoid | Urn | <20 μm overgrowths on Bn/Ccp in Chl-Qz-Cal veins | Chl-Cal-Bn/Ccp |
| Kult-82 | 546245, 6800094 | K82-10 | Basement granitoid | Urn-Uph * | 10 μm blebs integrown with lath-like Hem in Hem-Ser-Chl breccia matrix | Hem-Ser-Chl |
| Island | 0540868, 6803654 | I-12-1 | Basement granitoid + Gabbroic rock | Unknown | Fine-grained anhedral masses (<20 μm) with Gn in pits, overprinting Rt in quartz-chlorite veins | Chl-Gn |
| Pyramid | 0543655, 6793727 | PY-1 | Basement mafic gneiss | Unknown | U minerals not observed | |
| Cole | 0546116, 6800677 | C-02-2 | Granite-pebble conglomerate (Hjalmar Fm) | Unknown | Aggregate of <2 μm rounded grains | Chl-Ser-Hem |
| Welch | 0540821, 6802158 | W-01-1 | Sandstone (Taltson Fm) | Unknown | micro-inclusions in lathy Hem overprinting Rt and as very fine-grained disseminations in stringers with Gn | Chl-Ser-Hem-Gn |
| Dussault | 0540845, 6801729 | D-05 | Sandstone (Taltson Fm) | Unknown | Vug infilling polymetallic mineralization, intergrown with Gn | Chl-Ccp-Gn-Bi |

Abbreviations: bornite (Bn), calcite (Cal), chalcopyrite (Ccp), chlorite (Chl), Formation (Fm) galena (Gn), hematite (Hem), quartz (Qz), rutile (Rt), sericite (Ser), uraninite (Urn), and uranophane (Uph); * Determined using EPMA—See Section 4.2.

### *3.2. Petrographic Observations*

Thirteen variably altered samples were sent to Precision Petrographics in Langley, British Columbia, for sodium cobaltinitrite staining to aid in distinguishing potassic alteration (e.g., K-feldspar, sericite) from sodic alteration (e.g., albite).

Forty-four polished thin sections were prepared at Precision Petrographics and characterized using an Olympus BX53M polarizing petrographic microscope in both transmitted and reflected light. Compositional and textural analyses of uranium-bearing phases, associated sulphides and alteration minerals were determined using a TESCAN MIRA 3 LMU Variable Pressure Schottky field emission scanning electron microscope (SEM) at Saint Mary's University (Halifax), equipped with an Oxford INCA 80 $mm^2$ silicon draft detector capable of quantitative analysis energy dispersive spectroscopy (EDS) and a backscattered electron (BSE) detectors for imaging. Measurements were conducted at a working distance of ~17 mm, with a beam current of 40 μA and accelerating voltage of 20 kV. Raw data (counts and keV) were processed using the INCA software package.

False color element distribution mapping was conducted using a Bruker M4 Tornado micro-X-ray florescence (micro-XRF) spectrometer at the Department of Earth Sciences, University of New Brunswick (Fredericton), to map element distribution within select hand

samples. Analyses were conducted under vacuum using a Rh source at an accelerating voltage of 50 kV and beam current of 600 µA focussed to a 20 µm spot size at a counting time of 30 ms/pixel. Data were processed using the Bruker M4 Tornado software to produce relative intensity maps.

### *3.3. Mineral Chemistry*

Targeted uranium minerals and chlorite grains in polished thin sections were cut out as rock wafers ~2–3 mm in width with a Dremel tool and mounted into 1-inch diameter epoxy pucks. The minerals were analyzed for major and minor oxides using a JEOL JXA8230 electron probe microanalyzer (EPMA) equipped with five wavelength dispersive spectrometers (WDS) at the University of Toronto. The ZAF method was used to correct for matrix effects.

The composition of uranium minerals was determined using 40 EPMA measurements from six uranium mineralized samples (K82-C1, K82-C2, K82-10, C-02-2, I-12-1, W-01-1) with an accelerating voltage of 15 kV, a beam current of 30 nA and a 1 µm focused beam. Counts of characteristic X-rays lines for each element were quantified by comparison with analyses of in-house standards: barite (Ba$K\alpha$), bustamite (Mn$K\alpha$), $CePO_4$ (Ce$L\alpha$), Cr-augite (Al$K\alpha$, Ca$K\alpha$, Mg$K\alpha$, Si$K\alpha$), $DyPO_4$ (Dy$L\alpha$), $ErPO_4$ (Er$L\alpha$), $EuPO_4$ (Eu$L\alpha$), galena (Pb$M\alpha$), $GdPO_4$ (Gd$L\alpha$), hematite (Fe$K\alpha$), $HoPO_4$ (Ho$L\alpha$), $LaPO_4$ (La$L\alpha$), $LuPO_4$ (Lu$L\alpha$), $NdPO_4$ (Nd$L\alpha$), $PrPO_4$ (Pr$L\alpha$), sanidine (K$K\alpha$), $SnPO_4$ (Sm$L\alpha$), $TbPO_4$ (Tb$L\alpha$), $ThSiO_4$ (Th$M\alpha$), $TiO_2$ (Ti$K\alpha$), $TmPO_4$ (Tm$L\alpha$), tugtupite (Cl$K\alpha$), $UO_2$ (U$M\alpha$), $YPO_4$ (Y$L\alpha$), $YbPO_4$ (Yb$L\alpha$). Background and peak counting times were 10 and 20 s, respectively, for all elements except for REE, Fe and Mg (20 and 40 s, respectively), Si and Al (15 and 30 s) and K (5 and 10 s).

The chemical U-Th-Pb ages of uranium minerals were determined using the method by Bowles [39,40]. Time (t) was iteratively calculated via the equation $Pb = {}^{238}U(e^{\lambda U238t} - 1) + {}^{235}U(e^{\lambda U235t} - 1) + Th(e^{\lambda Th} - 1)$ using concentrations of U and Pb determined by EPMA and an assumption that the uranium obtained consists of 99.276% $^{238}U$ and 0.0155125% $^{235}U$.

Chlorite grains from unmineralized and mineralized samples were analyzed with an accelerating voltage of 15 kV, a beam current of 10 nA and a 15 µm beam diameter. Counts of each element were quantified using counts produced by known standards and energy lines: albite (Na$K\alpha$), bustamite (Ca$K\alpha$, Mn$K\alpha$), chloriteSx2 (Al$K\alpha$, Si$K\alpha$), chlorite_118 (Mg$K\alpha$), $Cr_2O_3$ (Cr$K\alpha$), hematite (Fe$K\alpha$), $MgF_2$_halide (F$K\alpha$), pentlandite (Ni$K\alpha$), sanidine (K$K\alpha$), $SrTiO_3$ (Sr$L\alpha$), $TiO_2$ (Ti$K\alpha$) and tugtupite (Cl$K\alpha$). Background and peak counting times were 10 and 20, respectively, for all elements except for K, Na, F, Cr (5 and 10 s, respectively) and Mn (20 and 40 s, respectively).

The chemical formula of chlorite was calculated based on the ideal composition of chlorite, $(R_w{}^{2+}R_y{}^{3+}\square_z)^{VI}(Si_{(4-x)}Al_x)^{IV}O_{10}(OH)_8$, modified from Wiewióra and Weiss [41], where $w + y + z = 6$, and $\square$ represents structural vacancies. Octahedral (VI) sites house divalent cations ($R^{2+}$), primarily $Mg^{2+}$ and $Fe^{2+}$, as well as trivalent ($R^{3+}$) cations, such as $Al^{3+}$ and $Fe^{3+}$ [41]. Tetrahedral (IV) sites host $Si^{4+}$ in four tetrahedral positions, where $x$ is the number of trivalent cations (e.g., $Al^{3+}$) substituting for $Si^{4+}$. For cation site assignment, the tetrahedral site is first filled with $Si^{4+}$ then $Al^{3+}$ to sum 4 cations. Temperatures were calculated using stoichiometric calculations and the chlorite geothermometry equation $T(°C) = -61.92 + 321.98(Al^{IV})$, where $Al^{IV}$ is Al content in the tetrahedral site [42]. Additionally, a more recent graphical chlorite thermometer by Bourdelle and Cathelineau [42] was used to confirm the temperatures and this yielded similar results. These geothermometers were deemed appropriate as they are intended for low temperature, diagenetic, metamorphic and hydrothermal chlorite.

### *3.4. Whole-Rock Geochemistry*

A total of thirty-six representative host rock and mineralized samples were selected for whole-rock geochemistry. Sample preparation and analysis were performed at Activation Laboratories Inc. in Ancaster, ON, Canada. Major elements were analyzed using X-ray fluorescence (XRF) on metaborate fusion glass pellets. Trace elements were analyzed using

Inductively Coupled Plasma Mass Spectrometry (ICP-MS) and Inductively Coupled Plasma Optical Emission Spectrometry (ICP-OES) on samples prepared using a closed vessel multi-acid digestion. Various standards were analyzed to ensure accuracy and precision of data, as well as duplicates unknown every 10 samples.

## 4. Results

### *4.1. Petrography and Paragenesis*

Similar alteration mineral assemblages were observed at the uranium occurrences studied, despite having different host-rocks and variable modes of occurrence (Table 1). Additionally, the paragenetic sequence of these assemblages are consistent and summarized in Figure 3. A summary of the styles and modes of uranium mineralization for the different occurrences (Kult-82, Island, Cole, Welch and Dussault), including uranium mineral species determined by EPMA, associated mineral assemblages, phases of chlorite, and host lithologies is presented in Table 1.

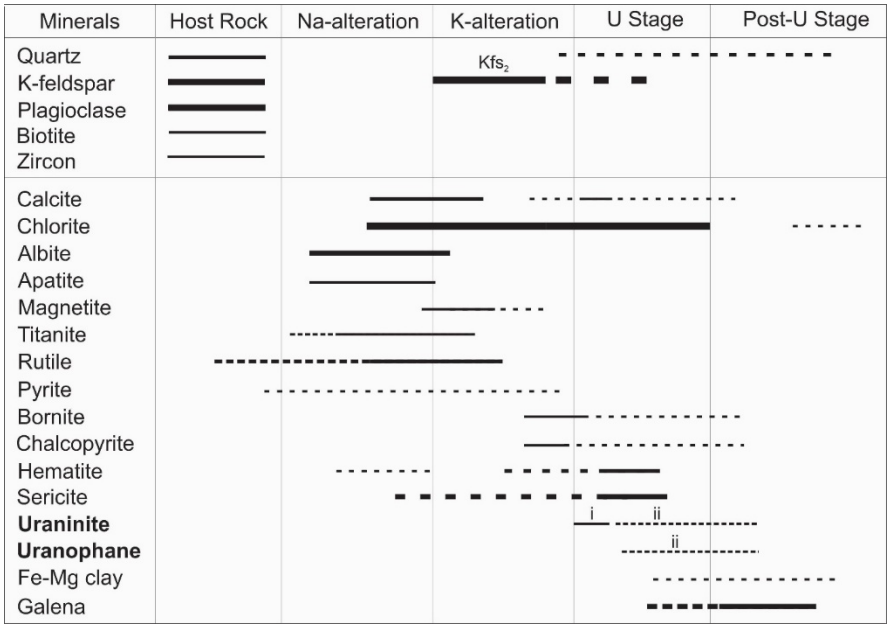


**Figure 3.** Mineral paragenesis of uranium occurrences at MacInnis Lake, Nonacho Basin. Weight of lines indicate relative abundance and dashed lines represent uncertainty in the sequence. Abbreviations: K-feldspar alteration ($Kfs_2$).

#### 4.1.1. Basement Hosted Uranium Occurrences

Kult-82

The Kult-82 occurrence is hosted within a basement granitoid consisting predominantly of coarse-grained to pegmatitic intermediate-sodic plagioclase ($Ab_{53–85}$), microcline and quartz, with interstitial biotite, partially pseudomorphed by chlorite (Figure 4a). Distal from deformation zones and lithological contacts, the granitoids are dark pink to brick-red in colour and have undergone sodic alteration (Figure 4a), whereby plagioclase and microcline are pseudomorphically altered to secondary albite ($Ab_{93–100}$). Proximal to lithological contacts and deformation zones, the albitized granitoids are overprinted by brick-red potassic alteration consisting of fine-grained, hematized Ba-rich K-feldspar, and very fine-grained interstitial sericite, that is also locally inter-grown with chlorite in veins. Secondary blebby quartz commonly occurs with the K-feldspar. Veins of sericitized black chlorite ± calcite crosscut the granitoids and earlier phases of alteration (Figure 4b). Remobilized uranium mineralization is evident by yellow radioactive surface staining (likely uranophane) along black chloritized fracture surfaces in outcrop and in hand specimens (Figure 4c).

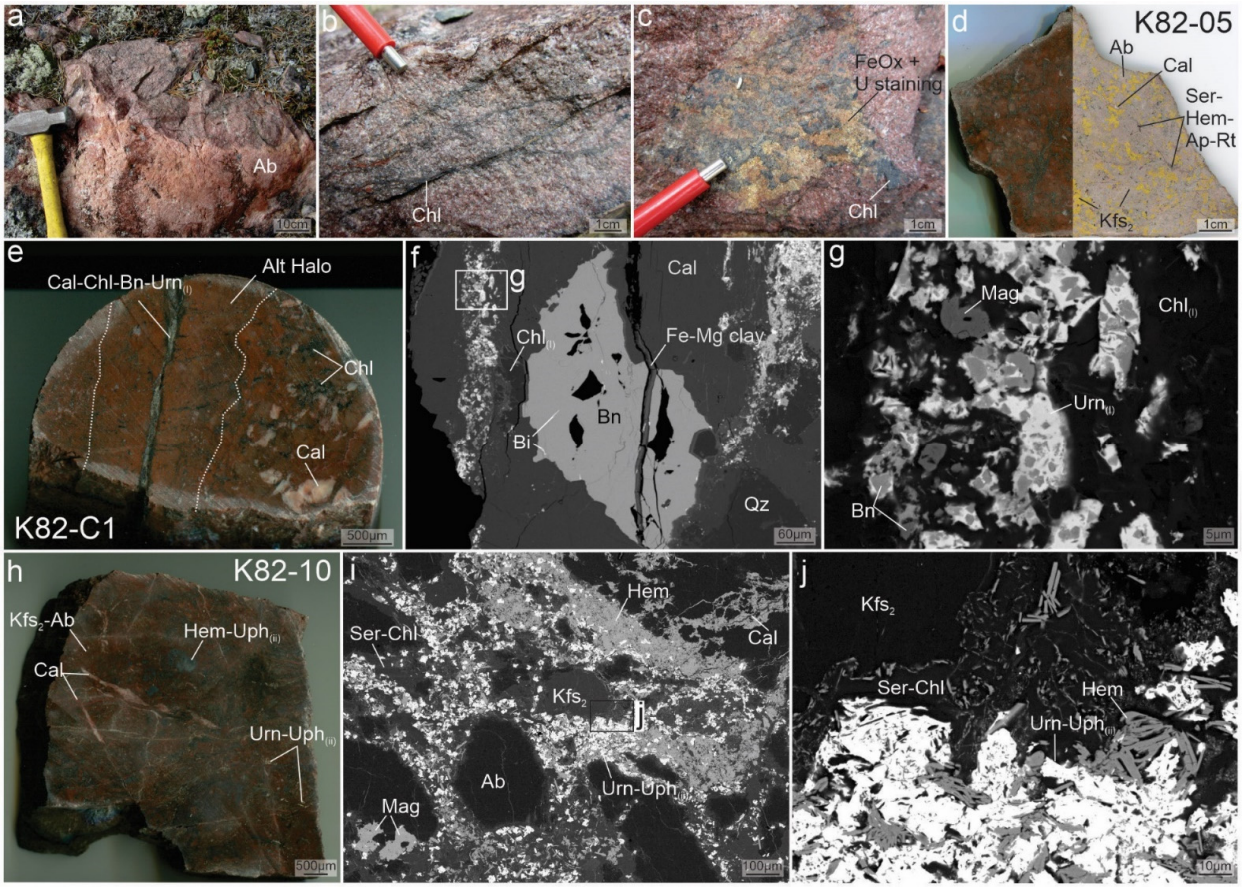


**Figure 4.** Images of the host rocks and uranium minerals at the Kult-82 occurrence. (**a**) pink albitized granitoid host rock; (**b**) mm-scale black chlorite (Chl) veins; (**c**) chlorite on fracture surfaces coated with secondary Fe-oxide (FeOx) and yellow uranium staining; (**d**) sodium cobaltinitrite stained (right) granitoid (K82-05) showing pervasive albitization (Ab; pink) overprinted by Ba-rich K-feldspar ($Kfs_2$; yellow) alteration, as shown with staining; (**e**) sample K82-C1 with a very fine-grained albitized alteration halo (Alt Halo) surrounding a bornite (Bn), type-i uraninite (Uran) bearing type-i chlorite and calcite (Cal) vein; (**f**) SEM-BSE image of bornite in calcite with Bi-inclusions cross-cut by an unidentified ferro-magnesian mineral; (**g**) SEM-BSE image of type-i uraninite overgrowths on bornite with magnetite (Mag) in a chlorite-calcite vein; (**h**) sample (K82-10) hosting type-ii uraninite-uranophane ($Urn\text{-}Uph_{(ii)}$) in a hematite- sericite-chlorite (Hem-Ser-Chl) breccia with late calcite veins; (**i**) clasts of locally Ba-rich secondary K-feldspar and as well as minor blocky magnetite hosted in the hematite-sericite-chlorite matrix (from **h**); (**j**) SEM-BSE enhanced image of box in (**i**) showing inter-grown, coeval hematite-$Urn\text{-}Uph_{(ii)}$ in sericite-chlorite matrix.

Uranium mineralization is spatially associated with albitized and K-feldspar altered deformation zones that crosscut the altered granitoids close to the overlying unconformable contact with the Hjalmar conglomerates. There are two main styles of uranium mineralization (see Section 4.2 for details on uranium mineral classification): (i) type-I altered uraninite as overgrowths on partially dissolved Cu-sulphides and (ii) type-ii altered uraninite-uranophane disseminated within a hematite-sericite-chlorite breccia. The first style of uranium mineralization is hosted in the mm-scale black chlorite-calcite + quartz veins as overgrowths on partially dissolved Cu-sulphides (bornite in sample K82-C1, and, to a lesser extent, chalcopyrite in sample K82-C2) and as disseminated fine-grained (<20 µm) blebs (Figure 4e). Bornite occurs as both anhedral, coarse-grained (100–200 µm) inclusions in calcite, that contain laths of native Bi, and are cross-cut by a ferromagnesian clay mineral (potentially stilpnomelane or minnesotatite; Figure 4f). Bornite also occurs as fine-grained, anhedral blebs and is locally associated with altered uraninite and

minor subhedral magnetite (Figure 4f,g). The second style of uranium mineralization occurs in the matrix of a hematite-sericite-chlorite breccia (Figure 4h–j). Brecciated clasts include secondary albite ($Ab_{93–100}$) and minor secondary K-feldspar that is locally Ba-rich (Figure 4i). In the hematite-sericite-chlorite matrix, uranium mineralization occurs as anhedral grains (10–20 µm) coeval and inter-grown with bladed to lath-like hematite of similar size with a sericite-chlorite matrix (Figure 4i,j). Veinlets of calcite locally crosscut the breccia (Figure 4h,i).

Island

The Island occurrence is located along the western margin of MacInnis Lake and is hosted within a similar basement granitoid to the Kult-82 occurrence (Figure 2b, in addition to a younger gabbroic intrusion). A sharp contact between potassic altered granitoids and the gabbroic intrusion, as well as inclusions of the granitoid within the gabbro, are visible in outcrop (Figure 5a). Gandhi and Prasad [7] documented that the gabbro also crosscuts the sedimentary Taltson and Thekulthili formations of the basin; however, this could not be confirmed in the field by the authors of the current paper.

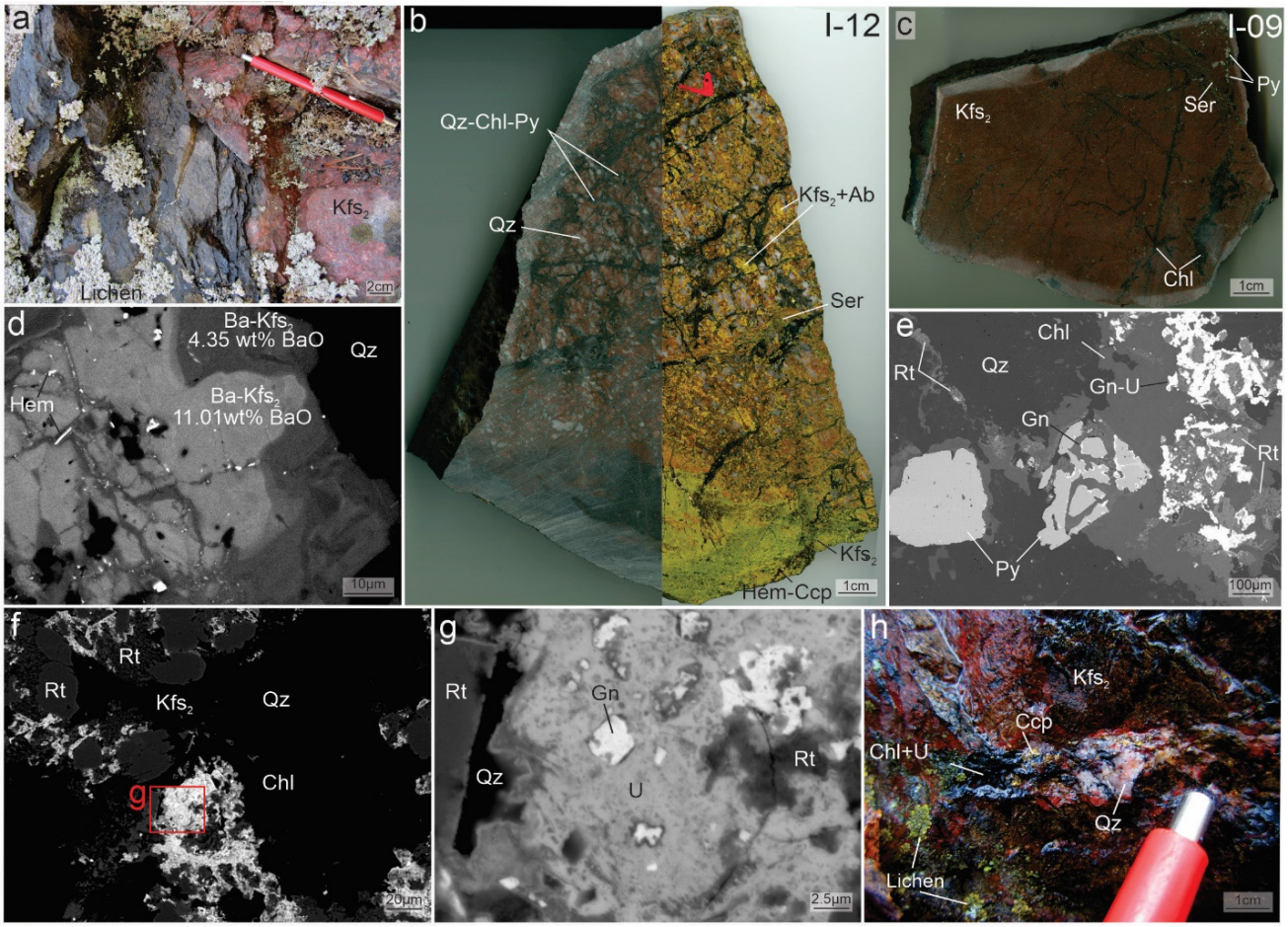


**Figure 5.** Host rocks and uranium minerals at the Island occurrence. (**a**) The contact between the gabbroic intrusion and brick-red K-feldspar altered ($Kfs_2$) granitoid. (**b**) Granitoid sample I-12 with sodium cobaltinitrite staining (right) shows the distribution of potassic (yellow) and sodic (pink) alteration. The majority of the sample is altered to a fine-grained secondary albite (Ab) overprinted by K-feldspar alteration with blebby quartz that is cross-cut by chlorite-sericite (Ser) veins ± quartz and euhedral pyrite (Py). The lower portion of the slab is composed of very fine-grained K-feldspar alteration with veinlets of chalcopyrite and hematite (Hem). (**c**) Gabbro sample I-09 showing brick-red K-feldspar alteration, sericitized chlorite veins, and euhedral pyrite. (**d**) SEM-BSE image of sample I-09 where zoned Ba-rich K-feldspar contain laths and fracture-filled hematite. (**e**) A SEM-BSE image

of a quartz-chlorite vein from sample I-12 containing uranium (U) mineralization with galena (Gn) cross-cutting rutile (Rt) and pyrite. (**f**) An SEM-BSE image of a quartz-chlorite vein in sample I-12 containing K-feldspar alteration ($Kfs_2$) and blocky aggregates of rutile (Rt). (**g**) Uranium minerals with abundant galena inclusions and overprinting rutile in a quartz-chlorite vein. (**h**) Centimetre-scale vein of chlorite, quartz (Qz) with chalcopyrite (Ccp) and with black uranium mineral (uraninite?) in brick-red altered gabbro.

The least-altered granitoid is medium-grained, pink in colour and contains cm-scale quartz-feldspar veins with clots of magnetite and/or specular hematite. The granitoid has undergone similar alteration to the granitoid at the Kult-82 occurrence, where secondary albite and fine-grained hematized and Ba-rich K-feldspar alteration with blebby quartz are cross-cut by veins of quartz and locally sericite with black chlorite (Figure 5b). Near structures and lithological contacts, the granitoid has undergone pervasive potassic alteration manifested by very fine-grained, Ba-rich and brick-red secondary K-feldspar alteration. The brick-red and Ba-rich K-feldspar contains micro-inclusions of hematite (e.g., sample I-09; Figure 5c,d) and Ba-zonation with higher Ba in the core than the rim (Figure 5d).

The late quartz-chlorite veins commonly contain pyrite, chalcopyrite, hematite, rutile (Figure 5b) and local uranium mineralization (Figure 5e). The uranium minerals are spatially associated with two generations of rutile (earlier blocky and later aggregate; Figure 5e) and local pyrite, with galena rims (Figure 5e). The fine-grained disseminated uranium minerals contain abundant galena inclusions, and overprint aggregates of blocky rutile and local pyrite ± galena (Figure 5f,g).

The Island gabbro varies from fine- to coarse-grained and is locally epidote altered. The gabbro is brick-red in areas where secondary hematized Ba-rich K-feldspar alteration is pervasive. Secondary K-feldspar also occurs along the margins of 1–2 cm wide veins of quartz, black chlorite and calcite that contain a highly radioactive black mineral, tentatively identified as uraninite (Figure 5h). Although these veins were exposed in outcrop, no intact samples could be collected with the available hand tools.

Pyramid

The Pyramid occurrence is located on the southern tip of MacInnis Lake (Figure 2b). There are three main lithologies in the area: (i) felsic gneisses, which have been intruded by (ii) pegmatite dikes (Figure 6a), and (iii) mafic gneisses, which have been variably chloritized and host uranium minerals (Figure 6b,c). The felsic gneiss is coarse grained and light pink in color. The pegmatitic intrusions consist of euhedral K-feldspar and minor quartz, which are cross-cut by black chlorite veins. The mafic gneiss is fine-grained, weakly magnetic, pervasively chloritized, variably clay altered, and silicified (Figure 6b,c). Veins of vuggy quartz infilled by wispy calcite crosscut the host in various locations (Figure 6b). Clasts of basement granitoid, which contain disseminated pyrite and minor chalcopyrite, are suspended in the chloritized gneiss (Figure 6c).

The Pyramid occurrence is hosted in brecciated mafic gneiss where veins of cm-scale cox-comb quartz are infilled with wispy calcite (Figure 6d). The quartz-calcite veins and brecciated mafic gneiss are radioactive, and yellow secondary uranium mineral staining and Fe-oxide weathering are common in exposed outcrops (Figure 6e). An alteration halo surrounds the breccia zone where the mafic gneiss is highly silicified and chloritized. Although uranium mineralization was previously identified by Gandhi and Prasad [7] and radioactivity was high while conducting field observations, no uranium minerals were identified during petrographic observations of thin sections. The radioactivity within the samples is likely from surface staining by yellow secondary uranium minerals.

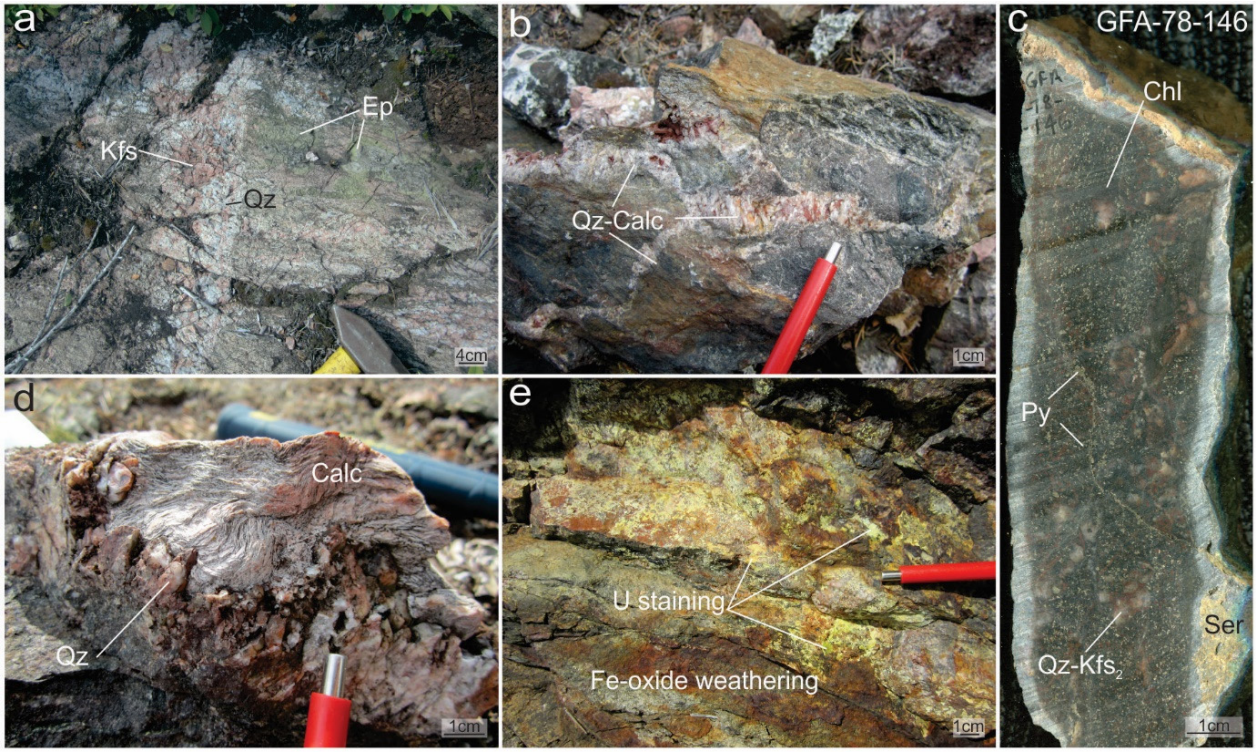


**Figure 6.** Representative lithologies and mineralized samples at the Pyramid occurrence: (**a**) Pegmatitic quartz (Qz) and K-feldspar (Kfs) vein crosscutting granitic gneiss with epidote (Ep) alteration of feldspars; (**b**) Vuggy quartz veins infilled with calcite (Calc) cross-cutting host amphibolite; (**c**) Clasts of quartz and secondary K-feldspar ($Kfs_2$) in highly chloritized matrix with sericite (Ser) infilling fractures and disseminated pyrite (Py); (**d**) Wispy calcite infilling cox-comb quartz vein; (**e**) Yellow secondary uranium staining and Fe-oxide weathering products are prominent near quartz-calcite veins in outcrop.

#### 4.1.2. Sediment Hosted Uranium Occurrences

Cole

Mineralization at the Cole occurrence occurs in shear and breccia zones cross-cutting the basal granite-pebble conglomerate of the Hjalmar Formation, near the unconformable contact with the basement granitoid (Figure 2b). The conglomerate contains cm-scale, sub-angular to sub-rounded clasts of basement granitoid within a chloritized greenish grey arkosic sandstone matrix (Figure 7a). The underlying basement granitoids are also weakly sheared and K-feldspar altered (Figure 7b). Conglomerates contain milled and rounded granitic clasts that have undergone secondary albite and potassic alteration, similar to basement granitoid rocks at the Kult-82 and Island occurrences. The milled clasts in sheared conglomerates are suspended in a sericitized chlorite matrix (Figure 7c).

The conglomerates contain quartz breccias that locally host uranium mineralization (Figure 7d,e). The matrix of mineralized breccia consists of quartz and variably sericite-chlorite with calcite, pyrite, hematite, apatite, rutile, titanite and minor uranium minerals (Figure 7d,e). Uranium minerals occur as small (1–2 μm) disseminated, rounded grains overgrown by hematite and spatially associated with bladed to lath-habit hematite in the sericite-chlorite matrix (Figure 7e–i). Veinlets of an unidentified ferromagnesian clay mineral with a similar composition to the unidentified mineral at the Kult-82 occurrence (i.e., stilpnomelane or minnesotatite), overprints sericitization, crosscuts granitic clasts, and exploits fractures in the quartz matrix (Figure 7f,g).

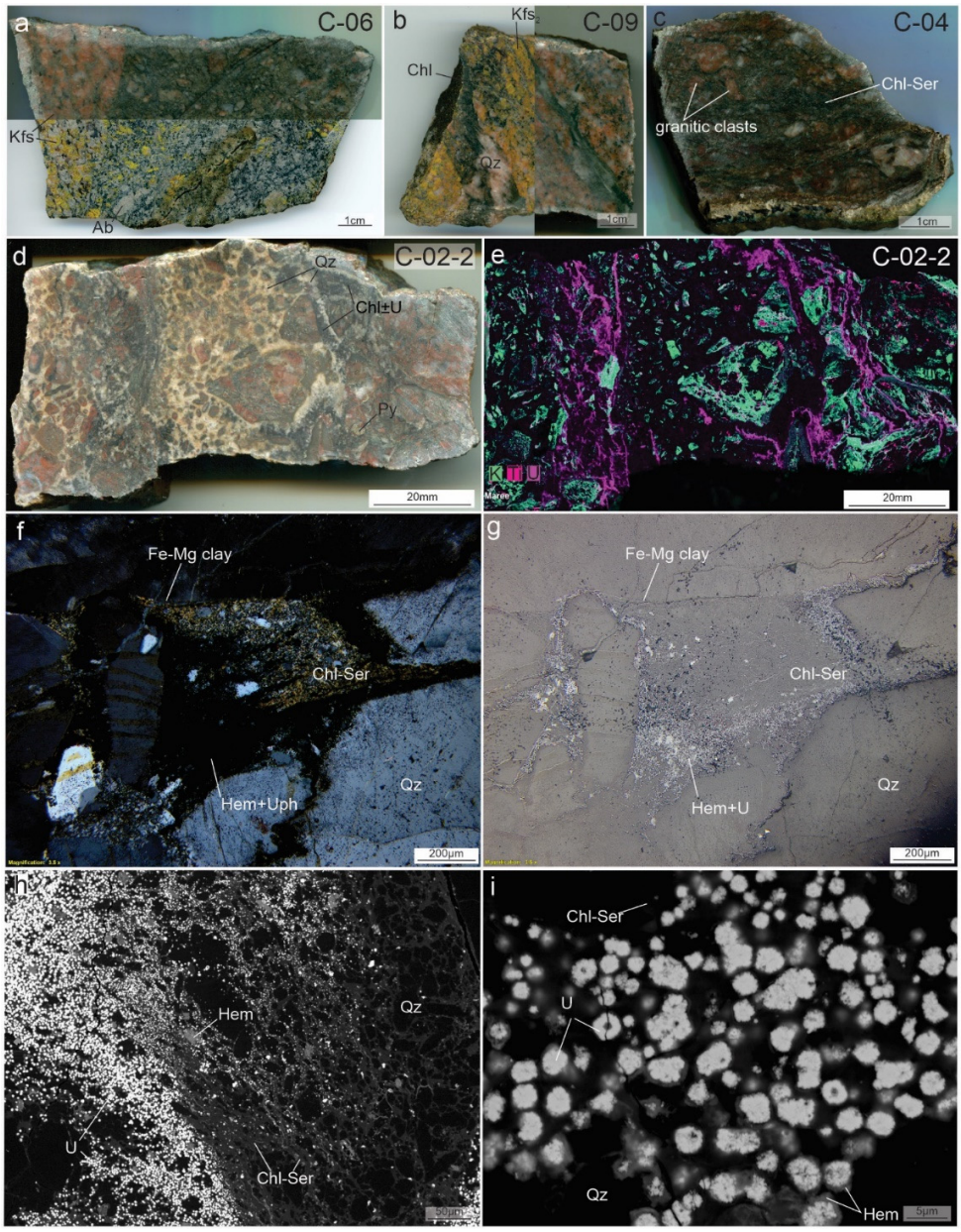


**Figure 7.** Host rocks and mineralization at the Cole occurrence. (**a**) Granite-pebble conglomerate of the Hjalmar Formation (sample C-06) showing sodium cobaltinitrite staining (bottom) and unstained surface (top) with clasts of predominantly secondary K-feldspar (Kfs) and albite (Ab). (**b**) K-feldspar altered ($Kfs_2$) and sericitized basement granitoid (sample C-09) stained with sodium cobaltinitrite (left) with cross-cutting black chlorite (Chl) and quartz (Qz) veins. (**c**) Foliated and brecciated conglomerate (sample C-04) with milled and rounded granitic clasts suspended in a black matrix of sericite (Ser) and chlorite. (**d**) uranium-mineralized quartz-sericite-chlorite breccia (sample C-02-2) where chlorite veins contain pyrite, rutile, hematite, and uranium minerals; (**e**) False color elemental map of (**d**) produced by micro-XRF showing the distribution of K (green), Ti (purple) and uranium (pink). (**f**) cross-polarized transmitted light photomicrograph of uranium minerals (U) with hematite (Hem) in chlorite-sericite veins within the breccia, crosscut by an unidentified ferromagnesian clay mineral; (**g**) reflected light photomicrograph of (**f**); (**h**,**i**) SEM-BSE images of very fine-grained bladed hematite with rounded uranium minerals associated with sericitized chlorite in the breccia.

### Welch and Dussault

The Welch and Dussault occurrences are hosted in the Taltson Formation, ~600 m apart, located along the western shoreline of MacInnis Lake (Figure 2b). The interbedded

sandstone-mudstone units of the uppermost Taltson Formation are composed of alternating layers of medium, to fine-grained pink arkosic sandstone, and greenish-grey mudstone. The sedimentary rocks are deformed in shear zones, displaying minor folding and crenulations and are broadly crosscut by a large network of quartz veins spanning up to 5 m wide (Figures 8a and 9a). Locally, the Welch and Dussault occurrences are highly brecciated by vuggy quartz veins that contain black chlorite-sericite and locally coated by yellow secondary uranium minerals (Figure 8a). Sericite is also common along fracture surfaces and along quartz vein margins (Figures 8b and 9c). Despite their similar host and proximity, the mineralogy of the uranium-bearing quartz veins at each occurrence is slightly different.

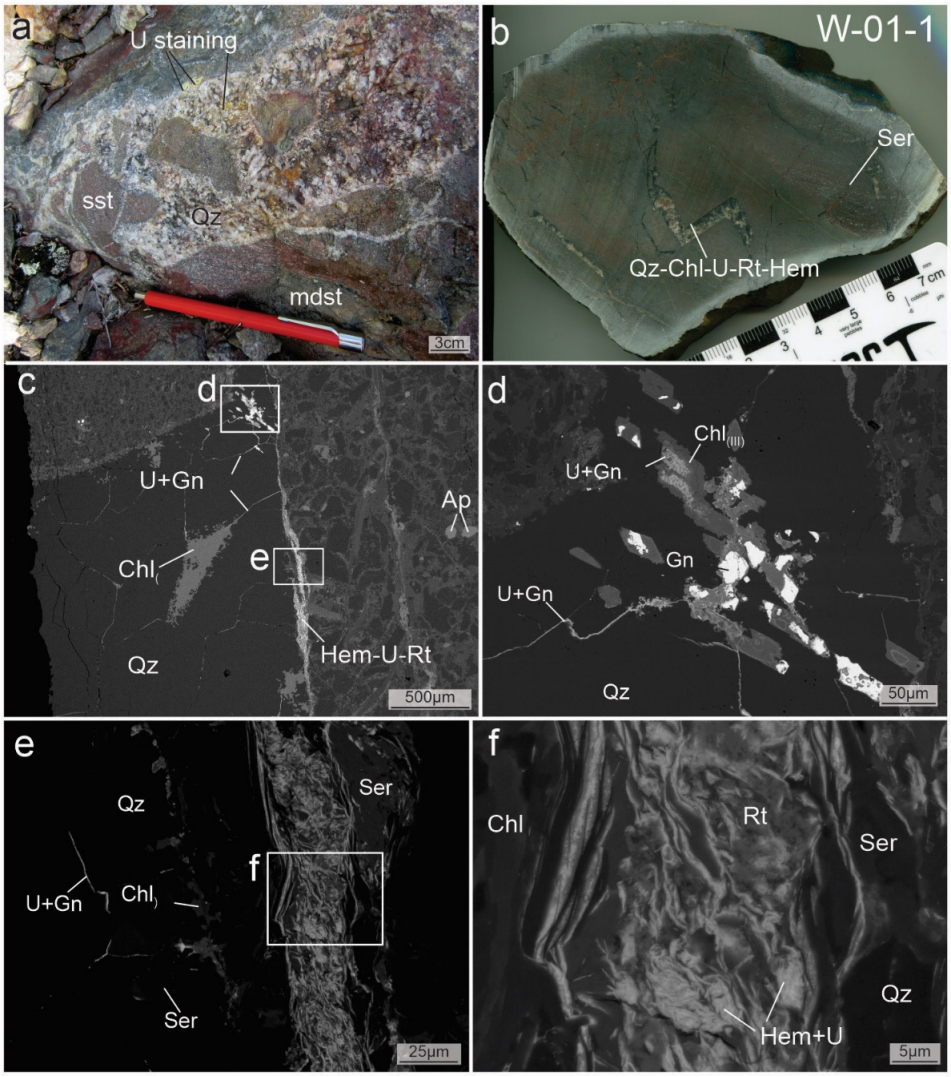


**Figure 8.** Host rocks and uranium mineralization at the Welch occurrence. (**a**) Interbedded sandstone (sst) and mudstone (mdst) brecciated by vuggy quartz (Qtz) veins and local yellow secondary uranium mineral staining. (**b**) Sample W-01 with vuggy quartz veins bordered by chlorite (Chl) containing rutile (Rt), hematite (Hem) and minor uranium mineralization. (**c**) A SEM-BSE image of the chloritize-sericite matrix in sample W-01 that contains early apatite (Ap) crosscut by a quartz vein containing rutile, hematite, and minor uranium mineralization along vein margins. Stringers of uranium minerals and galena follow quartz grain boundaries overprinting chlorite. (**d**) SEM-BSE image of chlorite overprinted by galena with local uranium in the cross-cutting quartz vein. (**e**) A SEM-BSE image of sericite and chlorite along the margin of quartz vein and stringers of uranium minerals with galena following quartz grain boundaries. (**f**) SEM-BSE image of box outlined in (**e**) showing lath-habit hematite containing micro-inclusions of uranium minerals and overprinting rutile associated with sericite-chlorite along quartz vein margins.

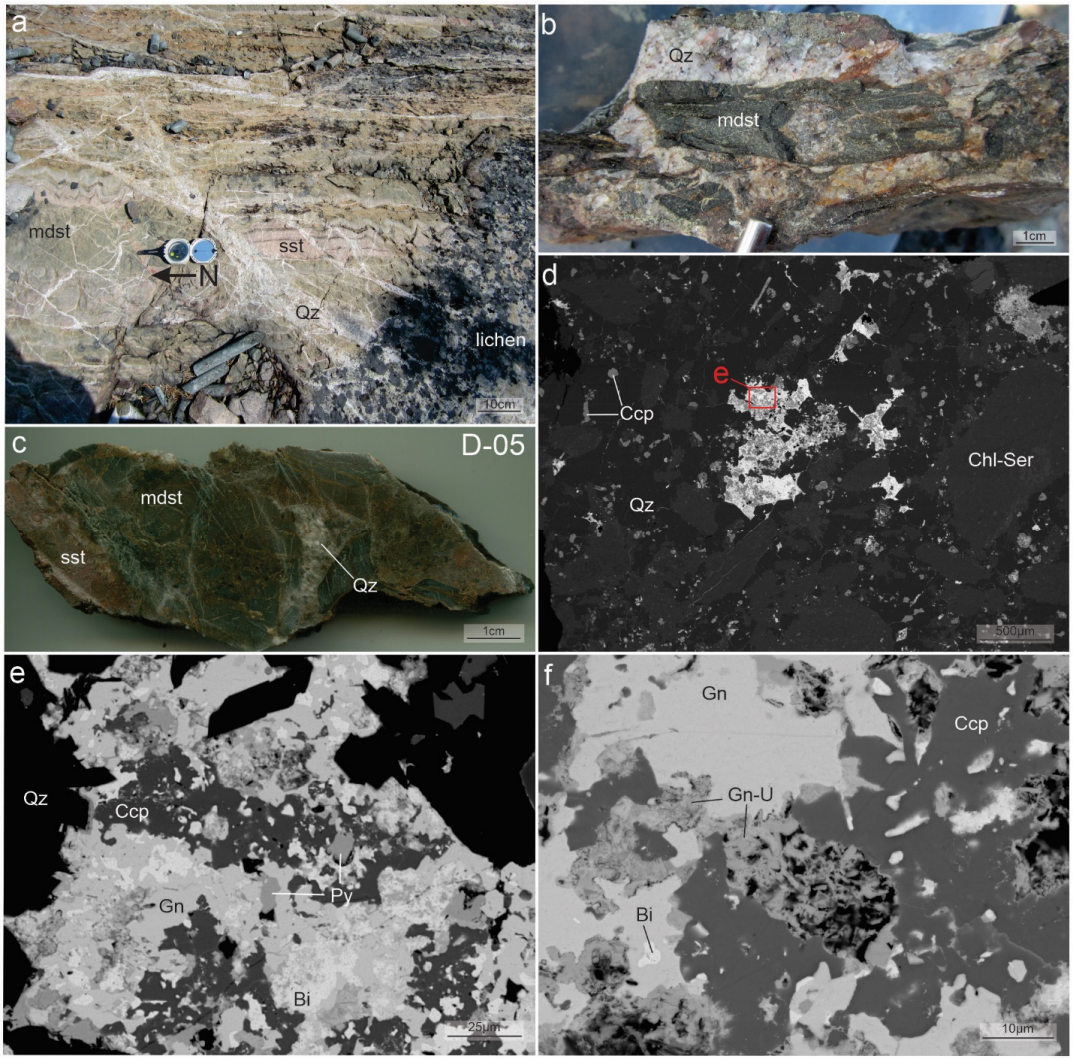


**Figure 9.** Host rocks and mineralization at the Dussault occurrence. (**a**) Interbedded sandstone (sst) and mudstone (mdst) of the Taltson Formation cross-cut by networking quartz (Qz) veins. Bedding is locally folded and deformed. (**b**) Quartz breccia sample D-05 with mudstone clasts, local Fe-oxide weathering and yellow uranium staining. (**c**) Sample D-05, showing vuggy quartz veins brecciating mudstone and sandstone. (**d**) A SEM-BSE image of vug-infilling chalcopyrite (Ccp) and polymetallic mineralization (box e) with chlorite (Chl) and sericite (Ser) altered clasts in quartz breccia. (**e**) SEM-BSE image from box e in (**d**) showing inter-growth of chalcopyrite, galena (Gn), pyrite (Py), native bismuth (Bi) and uranium minerals infilling vugs in quartz breccia. (**f**) SEM-BSE image of uranium minerals (U) and galena inter-growth.

At the Welch occurrence, the host sedimentary unit has undergone chloritization, sericitization and locally Ba-rich K-feldspar alteration. The chloritized and sericitized sedimentary matrix host apatite and veinlets of lathy hematite (Figure 8c). The host rock is cross-cut by networking vuggy quartz veins containing chlorite, rutile, hematite, galena, and minor uranium minerals (Figure 8c–f). The uranium minerals occur as micro-inclusions in lath-habit hematite, which surround rutile (Figure 8f). The uranium minerals and hematite are concentrated along the margins of quartz veins, associated with sericite-chlorite (Figure 8c,e). Galena occurs as disseminations and stringers containing micro-inclusions of uranium minerals interstitial to subhedral quartz grains of the veins (Figure 8c–e). Locally associated with subhedral galena and minor uranium minerals is chlorite exhibiting a vermiform texture (Figure 8c,d).

The Dussault occurrence is hosted in interbedded pebbly arkosic sandstone and red-green sandstone-mudstone units. The sedimentary units are locally deformed by folding and crosscut by large-scale, pervasive networking quartz veins (Figre 9a). Where mineralized, the sedimentary rocks are highly brecciated by vuggy quartz veins with sericite along fracture surfaces. Secondary yellow uranophane and Fe-oxide weathering are common along fracture surfaces (Figure 9a). Vuggy quartz veins contain abundant disseminations of chalcopyrite, interstitial to sericite-chlorite (Figure 9b–d). Polymetallic mineralization is evident in some vugs consisting of uranium minerals inter-grown with galena and overprinting chalcopyrite containing islands of native Bi (Figure 9e,f). Blebs of subhedral pyrite locally overprint chalcopyrite and galena (Figure 9e).

### *4.2. Uranium Mineral Chemistry*

The fine-grained nature of the uranium minerals and inter-growth with surrounding phases (e.g., chlorite, sericite, galena, quartz, hematite and rutile) limited EPMA analyses and data from many analytical points were discarded due to contamination from surrounding phases, including Cu-sulfides and silicates. Fifteen analyses from Kult-82 samples are presented in Table 2.

In general, the uranium minerals contain 61.55–81.09 wt.% $UO_2$ and variable to high concentrations of Si (0.83 to 12.08 wt.% $SiO_2$), Ca (1.33 to 4.39 wt.% CaO), Ba (0.46 to 3.50 wt.% BaO), Ti (0.14 to 1.55 wt.% $TiO_2$), Fe (1.23 to 3.61 wt.% FeO), Pb (<8.19 wt.% PbO), S (<2.26 wt.% $SO_3$), Y (<3.87 wt.% $Y_2O_3$), Ce (<2.29 wt.% $Ce_2O_3$) and Dy (<0.66 wt.% $D_2O_3$). They are variably hydrous, with totals as low as 92.51 wt.%). Notably, Th and many REE (Eu, Tb, Er, Tm, Yb, Lu) concentrations are less than detection limit.

The two styles of uranium minerals from the Kult-82 occurrence, (i) vein hosted uranium minerals as overgrowths on partially dissolved Cu-sulphides (K82-C1, K82-C2; Figure 4f) and (ii) granular blebs in a hematite-sericite breccia (K82-10; Figure 4i), are chemically distinct. Both styles of uranium mineralization at Kult-82 appear compositionally heterogeneous, as demonstrated by their variable distribution in CaO-$SiO_2$-$UO_2$ ternary diagram that aids in the classification of uranous and uranyl minerals, such uraninite ($UO_2$), coffinite ($U[SiO_4]\cdot nH_2O$), and uranophane ($Ca[UO_2]_2[SiO_3OH]_2\cdot 5H_2O$), (Figure 10). Fields for the composition of natural uraninite, coffinite and uranophane, confirmed by XRD [43], from the Centennial deposit of the Athabasca Basin are also plotted for comparison. Other common uranyl hydroxide minerals such as becquelerite ($Ca[UO_2]_6O_4[OH]_6\cdot 8H_2O$) and calciouranoite ($[Ca,Ba,Pb]U_2O_7\cdot 5H_2O$) were not included in the classification ternary, since these minerals contain much higher $H_2O$ and/or OH (>20 wt.%) than MacInnis Lake uranium minerals (as indicated by EPMA totals).

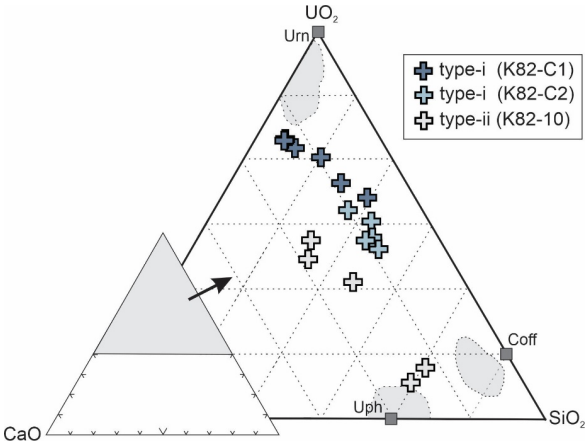


**Figure 10.** Molar proportions of major oxides in the uranium minerals at the Kult-82 (K82) occurrence plotted on CaO-$UO_2$-$SiO_2$ ternary diagram. The compositions of ideal uraninite (Urn), uranophane (Uph) and coffinite (Coff) are plotted, along with fields for these minerals from natural samples from the Centennial deposit in the Athabasca Basin [43].

**Table 2.** EPMA data (wt.% oxide) and calculated ages of uranium minerals of the Kult-82 occurrence.

| | Min [a] | $UO_2$ | PbO | $SiO_2$ | $TiO_2$ | $Al_2O_3$ | MgO | FeO | CaO | $K_2O$ | $P_2O_5$ | $SO_3$ | BaO | $Zr_2O_3$ | $La_2O_3$ | $Ce_2O_3$ | $Pr_2O_3$ | $Nd_2O_3$ | $Sm_2O_3$ | $Eu_2O_3$ | $Gd_2O_3$ | $Dy_2O_3$ | $Ho_2O_3$ | $Y_2O_3$ | $Er_2O_3$ | $Tm_2O_3$ | $Yb_2O_3$ | Total | $Ce_N/Y_N$ [b] | Age [c] | 2σ |
|---|---|---|---|---|---|---|---|---|---|---|---|---|---|---|---|---|---|---|---|---|---|---|---|---|---|---|---|---|---|---|---|
| K82-C1-1 | Urn | 70.69 | 0.87 | 3.06 | 0.58 | 0.19 | 0.06 | 3.61 | 1.69 | 0.02 | 1.07 | 1.56 | 0.94 | 0.54 | 0.40 | 1.81 | 0.31 | 1.25 | 0.47 | 0.06 | 0.36 | 0.66 | 0.102 | 3.87 | 0.116 | 0.10 | <0.16 | 94.35 | 1.3 | 213 | 9 |
| K82-C1-3 | Urn | 76.37 | 0.48 | 2.16 | 1.11 | 0.02 | 0.03 | 3.37 | 1.87 | 0.02 | 0.14 | 1.44 | 0.78 | 0.48 | 0.41 | 1.88 | 0.29 | 1.27 | 0.33 | 0.01 | 0.35 | 0.61 | 0.207 | 2.08 | 0.052 | 0.08 | <0.16 | 95.85 | 2.5 | 138 | 6 |
| K82-C1-4 | Urn | 76.99 | 2.37 | 0.83 | 1.55 | <0.03 | 0.02 | 3.58 | 2.46 | 0.01 | 0.09 | 1.4 | 0.46 | 0.20 | 0.55 | 2.02 | 0.23 | 1.14 | 0.32 | <0.16 | 0.43 | 0.60 | 0.12 | 2.15 | 0.017 | <0.15 | <0.16 | 97.52 | 2.6 | 509 | 20 |
| K82-C1-5 | Urn | 78.52 | 1.22 | 0.85 | 1.55 | <0.03 | 0.03 | 3.12 | 2.57 | 0.02 | 0.12 | 0.59 | 0.62 | 0.16 | 0.47 | 2.24 | 0.28 | 1.38 | 0.22 | <0.16 | 0.33 | 0.59 | 0.155 | 2.10 | 0.025 | 0.04 | 0.07 | 97.26 | 3.0 | 280 | 11 |
| K82-C1-6 | Urn | 74.66 | 1.07 | 4.37 | 0.62 | 0.27 | 0.12 | 3.37 | 1.33 | 0.03 | 0.15 | 1.30 | 1.12 | <0.08 | 0.41 | 2.29 | 0.21 | 1.41 | 0.39 | <0.16 | 0.19 | 0.60 | 0.16 | 1.72 | <0.14 | 0.05 | 0.11 | 95.95 | 3.7 | 253 | 10 |
| K82-C2-1 | Urn | 76.32 | <0.09 | 6.41 | 0.25 | 0.17 | 0.07 | 1.43 | 2.12 | 0.01 | 0.57 | <0.03 | 2.85 | 0.01 | 0.06 | 1.90 | 0.41 | 3.23 | 0.21 | 0.07 | 0.02 | 0.03 | <0.13 | 0.13 | <0.14 | <0.15 | 0.09 | 96.34 | 40 | | |
| K82-C2-2 | Urn | 79.84 | 0.07 | 5.52 | 0.18 | 0.26 | 0.03 | 2.05 | 1.81 | <0.04 | 0.21 | 0.01 | 1.85 | <0.08 | 0.12 | 1.65 | 0.41 | 2.76 | 0.26 | <0.15 | <0.11 | 0.11 | <0.13 | 0.06 | <0.14 | <0.15 | <0.16 | 97.20 | 75 | 60 | 2 |
| K82-C2-3 | Urn | 81.09 | <0.09 | 4.47 | 0.25 | 0.20 | 0.05 | 2.13 | 2.31 | 0.01 | 0.21 | <0.03 | 1.89 | <0.08 | 0.21 | 1.60 | 0.29 | 2.38 | 0.04 | <0.14 | 0.01 | 0.13 | <0.13 | 0.04 | <0.14 | <0.15 | <0.16 | 97.28 | 103 | | |
| K82-C2-4 | Urn | 75.53 | 2.35 | 5.75 | 0.31 | 0.29 | 0.06 | 1.87 | 2.03 | 0.04 | 0.34 | 1.29 | 2.20 | <0.08 | 0.16 | 1.63 | 0.48 | 2.67 | 0.07 | <0.14 | 0.05 | 0.11 | <0.13 | 0.04 | <0.14 | <0.15 | <0.16 | 97.26 | 116 | 508 | 20 |
| K82-C2-5 | Urn | 77.51 | <0.09 | 5.77 | 0.25 | 0.19 | 0.05 | 1.47 | 2.36 | 0.02 | 0.34 | <0.03 | 2.74 | <0.08 | 0.15 | 1.80 | 0.62 | 2.86 | 0.13 | 0.03 | <0.11 | 0.05 | 0.027 | 0.08 | <0.14 | <0.15 | <0.16 | 96.44 | 60 | | |
| K82-10-1 | Urn | 73.90 | 8.19 | 3.72 | 0.29 | 0.19 | 0.08 | 3.18 | 3.90 | 0.09 | 0.21 | 2.25 | 2.43 | 0.19 | 0.14 | 0.52 | 0.03 | 0.12 | 0.03 | 0.03 | <0.11 | 0.16 | <0.13 | <0.07 | <0.14 | <0.15 | <0.16 | 99.63 | >32 | 1757 | 70 |
| K82-10-2 | Uph | 61.55 | 7.84 | 11.88 | 0.18 | 1.85 | 0.09 | 1.21 | 4.16 | 0.21 | 0.09 | 2.26 | 2.44 | <0.08 | <0.21 | 0.53 | <0.16 | 0.12 | <0.14 | <0.14 | <0.11 | 0.03 | <0.13 | <0.07 | <0.14 | 0.03 | 0.06 | 94.54 | >36 | 1739 | 70 |
| K82-10-3 | Urn | 75.30 | 4.45 | 6.61 | 0.14 | 0.25 | 0.05 | 1.23 | 3.78 | 0.06 | 0.11 | 0.55 | 2.03 | <0.08 | <0.21 | 0.35 | 0.04 | 0.18 | 0.09 | <0.14 | <0.11 | 0.09 | <0.13 | <0.07 | <0.14 | <0.15 | 0.01 | 95.29 | >22 | 941 | 38 |
| K82-10-4 | Urn | 71.87 | 5.49 | 4.05 | 0.22 | 0.3 | 0.04 | 1.26 | 4.39 | 0.35 | 0.09 | 0.83 | 2.99 | 0.12 | 0.16 | 0.31 | <0.16 | 0.13 | <0.15 | <0.14 | <0.11 | 0.09 | <0.13 | <0.07 | <0.14 | <0.15 | <0.16 | 92.69 | >20 | 1170 | 50 |
| K82-10-6 | Uph | 64.44 | 3.30 | 12.08 | 0.19 | 2.02 | 0.35 | 2.65 | 3.27 | 0.09 | 0.13 | 0.04 | 2.89 | <0.08 | 0.11 | 0.38 | 0.08 | 0.08 | 0.01 | 0.04 | <0.11 | 0.23 | <0.13 | <0.07 | 0.012 | 0.09 | <0.16 | 92.51 | >15 | 711 | 30 |

Oxides below detection: $ThO_2$ (0.12 wt.%), $Tb_2O_3$ (0.13 wt.%), $Lu_2O_3$ (0.02 wt.%), Cl (0.04 wt.%) [a] Minerals: Urn = uraninite, Uph = uranophane. [b] Chondrite normalized using [44]. [c] Calculated using [39,40].

Type-i uranium minerals have high but variable U (70.69–81.09 wt.% $UO_2$) and Si (0.83–6.41 wt.% $SiO_2$), with consistent Ca (1.33–2.57 wt.% CaO). On the classification ternary, type-i uranium minerals form a trend that extends from uraninite toward ideal coffinite and uranophane and are classified as altered uraninite. Type-ii uranium minerals contain less U (61.55–75.30 wt.% $UO_2$) and higher Ca (3.27–4.39 wt.% CaO), Si (3.72–12.08 wt.% $SiO_2$) and Pb (3.30– 8.19 wt.% PbO) than type-i uranium (Table 2). Type-ii uranium has a more variable distribution in the classification ternary (Figure 10), extending to the uranophane field. Type-ii uranium minerals include altered uraninite with minor quantities of uranophane.

Overall, type-i altered uraninite has higher ΣREE+Y (4.70–9.51 wt.%) than type-ii altered uraninite-uranophane (0.69–1.05 wt.%; Table 2). The concentrations of Ce and Y are used as proxies for LREE and HREE concentrations, respectively, because (i) Ce is an abundant LREE in the uranium minerals of this study and (ii) Y is more abundant than HREE (which were usually near or below detection limit of the EPMA), while having similar geochemical behavior owing to its ionic radii and charge. Type-i uranium minerals can be subdivided into two groups based on distinctions in REE chemistry between samples K82-C1 and K82-C2. Sample K82-C1 has the highest $(\Sigma REE+Y)_2O_3$ (7.54–9.51 wt.%) and $Ce_N/Y_N$ ranges from 1–4, indicating chondrite normalized pattern would be relatively flat lying (Table 2; Figure S3). Sample K82-C2 contains lower $(\Sigma REE+Y)_2O_3$ between 4.70–6.15 wt.% but variably high $Ce_N/Y_N$ ratios (40–116; Table 2), indicate a negatively sloped chondrite normalized REE pattern. Also, Nd concentrations are higher than Ce in K82-C2 uranium minerals. Type-ii uranophane contains much less ΣREE+Y overall, with most element concentrations (Eu, Tb, Ho, Er, Tm, Yb and Lu) below detection; however, Ce is appreciable (~0.30 to 0.52 wt.% $Ce_2O_3$). Concentrations of Y below detection of 0.08 wt.% $Y_2O_3$ suggest ratios greater than 32.

A large range in chemical U-Th-Pb ages of uraninite from the Kult-82 were calculated (Table 2). The age of type-i uraninite ranges from 508 ± 20 Ma to <1 Ma. Type-ii uranium minerals are older, with the two oldest ages 1757 ± 70 Ma for uraninite and 1739 ± 70 Ma for uranophane.

### *4.3. Chlorite Thermometry*

The composition of chlorite associated with uranium mineralization from Kult-82, Cole and Dussault, as well as chlorite in albitized basement granitoid from Kult-82, is presented in Table S3. Although chlorite occurs with uranium mineralization at other showings, it was too fine-grained or inter-grown with sericite for analysis. The chlorites are Fe-rich and classify as chamosite based on proportions of octahedral Fe, Mg and Al.

At Kult-82, the chlorite occurs as fine-grained granular to acicular clusters in veins occurring with calcite, bornite, magnetite and type-i uraninite-uraninite mineralization (Figure 4e–g). Based on three analyses, it has an average Fe# of 0.70 and formed at approximately 323 ± 4 °C. Chlorite in unmineralized albitized granitoid of Kult-82 occurs as pseudomorphs of biotite and has a very similar composition (Fe# = 0.72) and temperature (329 ± 5 °C) to the chlorite with type-I uraninite.

Chlorite of the Cole and Welch occurrences occurs as worm-like clusters (Figures 7d,h and 8b–f) and occurs with sericite-hematite-uranium minerals ± quartz. At the Welch occurrence, it is also associated with galena. The Fe# average 0.66 ± 0.03 (n = 6) and 0.69 ± 0.04 (n = 8) and formed around 329 ± 8 and 314 ± 11 °C, respectively. Therefore, all chlorites exhibit similar Fe# and temperatures regardless of occurrence.

### *4.4. Whole-Rock Geochemistry*

Major and trace elements of variably altered and locally mineralized granitoids, mineralized sedimentary rocks and unmineralized host rocks are presented in Tables S4 and S5. In general, uranium mineralized granites and sandstones/mudstones exhibit variably high K/Na ratios reflecting potassic (K-feldspar, sericite) alteration spatially associated with uranium mineralization (Figure 11a), compared to unmineralized host rocks. Lower K/Na in mineralized gabbros and conglomerate reflect high amounts of sodic alteration (albite;

Figure 11a), while low K/Al and high Mg/Al reflect abundant chlorite (containing ~9 wt.% MgO; Table S1) with K-feldspar associated with mineralization in gabbroic rocks from the Island occurrence (Figures 5c and 11b). Both mineralized and unmineralized rocks show high and variable Ba, up to the upper detection limit of the ICP-MS (5000 ppm; Figure 11c). Mineralized rocks also show higher concentrations of Cu, Ag, and Au than unmineralized rocks (Figure 11d–f).

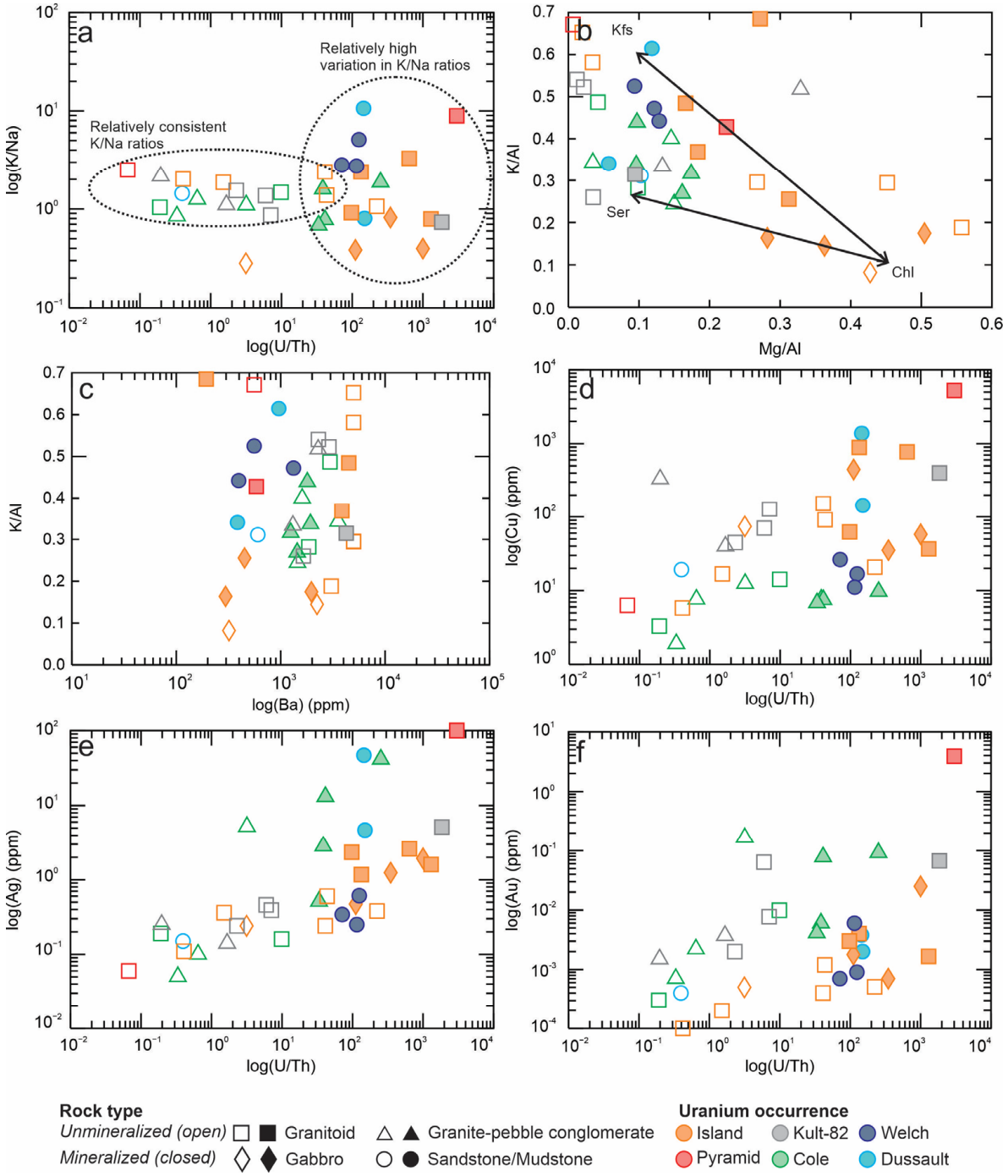


**Figure 11.** Bivariate diagrams using whole rock geochemical data for mineralized and non-mineralized rock types from various occurrences showing (**a**) U/Th vs. K/Na, (**b**) Mg/Al vs. K/Al, (**c**) Ba vs. K/Al, (**d**) U/Th vs. Cu, (**e**) U/Th vs. Ag, (**f**) U/Th vs. Au. Abbreviations: chlorite (Chl), K-feldspar (Kfs), sericite (Ser).

## 5. Discussion

### *5.1. Alteration Systematics and Paragenesis*

The underlying granitoids and younger sedimentary rocks of the MacInnis Lake area have undergone varying degrees of early alteration by albite and later, variably Ba-rich fine-grained K-feldspar. The replacement of primary plagioclase and microcline during pseudomorphic albitization increases the porosity of the mineral and, in turn, the host rocks, as the density of the newly formed albite is lower than that of plagioclase or microcline [45]. Additionally, grain-size reduction through replacement of feldspar by fine-grained K-feldspar, likely increased the porosity of crystalline basement rocks of the MacInnis Lake area. These mineralogical changes allowed for pervasive fluid flow responsible for the hydrothermal alteration and uranium mineralization observed in the area.

The altered unmineralized rocks are various shades of pink to brick-red. Although intense brick-red hues are typically diagnostic of hydrothermal K-feldspar in metasomatic environments [46], both pervasive albitization and K-feldspar alteration can have a brick-red appearance at MacInnis Lake (i.e., brick-red albitized granitoids at Kult-82; Figure 4d, e; and brick-red K-altered granitoids at Island; Figure 5c). This is attributed to the presence of fine-grained hematite in both secondary albite and K-feldspar (Figure 5d), where hematite is precipitated into nano-pores in potassic and/or sodic altered plagioclase under oxidizing conditions [47,48].

Early albitization of the host rocks can be modeled by the following reactions:

$$CaAl_2Si_2O_8 + Si^{4+}{}_{(aq)} + Na^{+}{}_{(aq)} \leftrightarrow NaAlSi_3O_8 + Al^{3+}{}_{(aq)} + Ca^{2+}{}_{(aq)} \quad (1)$$

$$KAlSi_3O_8 + Na^{+}{}_{(aq)} \leftrightarrow NaAlSi_3O_8 + K^{+}{}_{(aq)} \quad (2)$$

The addition of $Na^+$ in Equations (1) and (2) is not accounted for by the dissolution of an earlier phase in the host rock, considering plagioclase ($Ab_{53–85}$) is the dominate sodic phase; therefore, Na was likely provided by the fluid through metasomatic processes. Quartz dissolution provided $Si^{4+}$, as the albitized rocks are poor in quartz (Figure 4a). The granitoids are also vuggy and veined, both of which are infilled with calcite and lesser chlorite (Figure 4b,d,e). Pitted albite is commonly infilled with sericite, and biotite is pseudomorphically replaced by chlorite. It is likely that the calcite formed using the $Ca^{2+}$ provided by albitization of plagioclase. We attribute sericite formation in albite pores to the $Al^{3+}$ provided during albitization of plagioclase (Equation (1)), $K^+$ liberated during albitization of microcline (Equation (2)), as well as, $K^+$ and $H^+$ from the chloritization of biotite (Equation (3)). The latter reaction may occur as follows:

$$K(Fe_2Mg)AlSi_3O_{10}(OH)_2 + 2Fe^{2+}{}_{(aq)} + Al^{3+}{}_{(aq)} + 6H_2O_{(aq)} \leftrightarrow (Fe_4MgAl)AlSi_3O_{10}(OH)_8 + K^{+}{}_{(aq)} + 6H^{+}{}_{(aq)} \quad (3)$$

Based on the mineral assemblage (albite-sericite-chlorite-calcite) and calculations from Al in chlorite thermometry, the early Na-metasomatism that produced albite occurred at low hydrothermal temperatures (~330 °C; Table S1).

The Ba-rich, brick-red K-feldspar post-dates albitization, is commonly, but not always, associated with secondary blebby quartz. It is localized along structures and lithological contacts (e.g., the Island occurrence; Figure 5a), and sometimes exhibits zonation with higher Ba in the core than the rim (Figure 5d), suggesting this alteration event was facilitated by local K- and Ba-rich fluids. The K-feldspar altered granitoids and gabbros are cross-cut by veins of quartz-sericite-chlorite, that contain pyrite, chalcopyrite, hematite, rutile and locally, uranium mineralization associated with galena (Figures 4–6). Rutile is present as aggregates of blocky grains, possibly an alteration product of an earlier Ti-bearing ferro-magnesian mineral such as biotite.

Uranium mineralization at MacInnis Lake occurs in veins and breccia that post-date earlier albitization and Ba-rich K-feldspar alteration (Figures 3–9). No “fresh” uraninite was observed in this study, suggesting that primary uraninite was altered in-situ. The altered uraninite at Kult-82 incorporated substantial Si, Fe, Ca and Ba into its crystal structure

(Table 2). The incorporation of these elements into the crystal structure of uraninite is usually attributed to the substitution of radiogenic Pb during alteration events [21,22,49]. At Kult-82, Pb released during alteration was mobilized, whereas at the Welch, Dussault and Island occurrences, Pb was variably trapped as galena that forms inter-growths with uranium minerals (e.g., Figures 5g, 8d and 9f), indicating a higher sulfur fugacity in these showings [49,50]. High Ba concentrations (Table 2) were likely provided by the alteration of earlier Ba-rich K-feldspar, where rims contain low Ba contents relative to cores (Figure 5d).

Both uranium mineral types contain high REE and Y (Table 2). These elements were preserved during alteration and reflect the composition of the "fresh" earlier uranium minerals (likely uraninite). These elements are generally immobile in meteoric waters than can otherwise cause significant alteration to uranium minerals. Based on previous studies, secondary remobilized uranium minerals tend to contain similar to lower REE concentrations compared with primary uranium minerals [22,51].

Type-i and type-ii uranium minerals are differentiated by their respective composition, as well as timing and mineral associations (Table 2, Figures 3 and 10). Type-i uraninite contains relatively low Si and Ca relative to type-ii uraninite (Figure 10). Based on mineral associations and crosscutting relationships, we suggest that type-i uraninite, on partially dissolved Cu-sulphides, is older than type-ii uraninite associated with sericite and hematite (Figure 3). The low Pb concentrations of type-i uranium minerals (<2.37 wt.% PbO) and relatively younger ages (<508 Ma; Table 2), are interpreted to record recent alteration and Pb loss, and do not record the crystallization age of type-i uraninite mineralization. Type-ii uraninite-uranophane contains elevated Pb (3.30–8.19 wt.% PbO), indicating a minimum age of ~1750 Ma for type-ii uraninite and uranophane (Table 2).

The chemical distinction and mineral associations between type-i and type-ii uranium minerals, namely their Pb, Ca and Si concentrations (Table 2), and variability within the $CaO$-$SiO_2$-$UO_2$ ternary (Figure 10a), is likely due to two different mineralizing events. One of these produced type-i uraninite with chlorite on Cu-sulfides in veins at some unknown time, as younger alteration disrupted the U-Pb system. The other produced type-ii uranophane with sericite and hematite in breccias and gives ages between 1800 and 1700 Ma. This age range is significantly older than a previously reported whole rock $^{207}Pb/^{206}Pb$ age of 1073 Ma for MacInnis Lake uranium mineralization and slightly older than a 1617 Ma age for the Steve Showing of Thekulthili Lake area, 120 km south of MacInnis Lake [7]. The 1800–1700 Ma age range is consistent with strike-slip reactivation of the shear zones in the Nonacho Basin between 1830 and 1770 Ma [36]. Based on Al-in-chlorite thermometry, both type-i and type-ii uranium minerals formed at low temperatures, between 310–330 °C (Table S3).

### *5.2. Controls on Uranium Mineralization*

In general, uranium is highly soluble and mobile in its oxidized uranyl ($U^{6+}$) state; however, it must be reduced to its immobile, insoluble uranous ($U^{4+}$) state to form uraninite [52,53]. Reduction can occur through a variety of mechanisms, including anaerobic bacteria, graphite, organic matter, methane, hydrogen sulphide ($H_2S$) or the presence of reduced Fe in oxides, sulfides and silicate minerals (e.g., magnetite, pyrite, chlorite).

At the Kult-82 and Dussault occurrences, vein-hosted type-i uraninite (±galena) is texturally associated with partially dissolved Cu-sulphides, namely bornite and chalcopyrite (Figure 10). Considering the uranium minerals form overgrowths on the Cu-sulphides (Figures 4g and 9f), we suggest that reduced Fe in the sulphides acted as a reductant for primary uraninite precipitation. Oxidation of bornite can liberate reduced Fe as follows:

$$Cu_5FeS_{4\text{bornite}} + 7O_2 + 2H_2O = 5Cu^{2+}{}_{(aq)} + Fe^{2+}{}_{(aq)} + 4SO_4{}^{2-}{}_{(aq)} + 4H^{+}{}_{(aq)} \quad (4)$$

This reaction also produces abundant sulfate that may have been incorporated in uraninite during formation and/or subsequent alteration events. The redox reaction to produce uraninite may proceed following Equation (5).

$$UO_2Cl_2^{\circ}{}_{(aq)} + Fe^{2+}{}_{(aq)} = UO_2 + FeCl_2^{+}{}_{(aq)} \quad (5)$$

We propose that U(VI) was complexed with chloride, considering it is the most common ligand in hydrothermal systems, and saline sedimentary brines are commonly mineralizing fluids in similar temperature uranium deposits [54,55]. Hematite was not observed with type-i uraninite; therefore, ferric iron may have been soluble as a chloride complex.

Type-ii uraninite-uranophane occurs in hematite-sericite-chlorite breccia (Figure 4h–j). Early sulfides were not observed with type-ii uranium minerals; however, they are variably sulfate-rich (Table 2). It is possible that pre-existing sulfides were completely dissolved during the formation of this uraninite. Therefore, it may have formed through Equations (4) and (6).

$$5H_2O + U^{6+}{}_{(aq)} + 2Fe^{2+}{}_{(aq)} = UO_2 + Fe_2O_3 + 10H^{+}{}_{(aq)} \quad (6)$$

Considering hematite is inter-grown with type-ii uraninite (Figure 4h–j), ferric iron was insoluble.

### *5.3. Classification of Deposit Type*

Previous work by Gandhi and Prasad [7] suggest similarities in the geological context of the Nonacho Basin (i.e., fault-bound sedimentary basin unconformably overlying metamorphosed basement rocks) with Paleoproterozoic basins that host unconformity-type uranium occurrences, such as the Athabasca Basin and the Thelon Basin, which also overly the Rae craton (Figure 1). While similarities exist between the MacInnis Lake uranium occurrences and unconformity-type uranium deposits (primarily their proximity to the unconformity and low-temperature mineralization), we also note several key differences: (i) the MacInnis Lake uranium occurrences lack clay alteration (i.e., illite, kaolinite) and tourmaline, a prominent feature in unconformity-type uranium deposits of the Athabasca and Thelon basins [56–59]; (ii) the uranium minerals at MacInnis Lake are a mixture of altered uraninite ± uranophane, whereas uranyl minerals are commonly just alteration products of earlier uraninite in the Athabasca; and (iii) the chlorite associated with uranium minerals at MacInnis Lake are Fe-rich and relatively higher temperature (313–333 °C) than the ~200 °C sudoite in the Athabasca Basin [60]. Additionally, uranium overgrowths on early sulfides and hematite intergrowth with uranium minerals at MacInnis Lake suggests that $Fe^{2+}$ was the reductant for uranium mineralization, whereas sulfides in unconformity type uranium deposits are typically late [53,61–63]. Additionally, the REE+Y compositions of MacInnis Lake uranium minerals are high (over 10,000× chondrite) and with $Ce_N/Y_N$ ratios ≥ 1 (Table 2), while the compositions of unconformity-type uranium minerals contain substantially lower REE (between 10 and 1000× chondrite) and lower $LREE_N/HREE_N$ ratios than MacInnis Lake [20] (Figure 12). Although deposits of the Athabasca and Thelon basins have some similar structural and mineralogical features to the MacInnis Lake occurrences, we agree with previous studies that the likelihood of deposits comparable to unconformity-type uranium deposits is low for the Nonacho Basin [18,28]. Furthermore, the minimum age of Nonacho Group, constrained by the Sparrow Dike swarm (1827 Ma [64]), is considered to be too old for unconformity-type uranium deposits that are said to have formed globally after ~1.75 Ga [18,52].

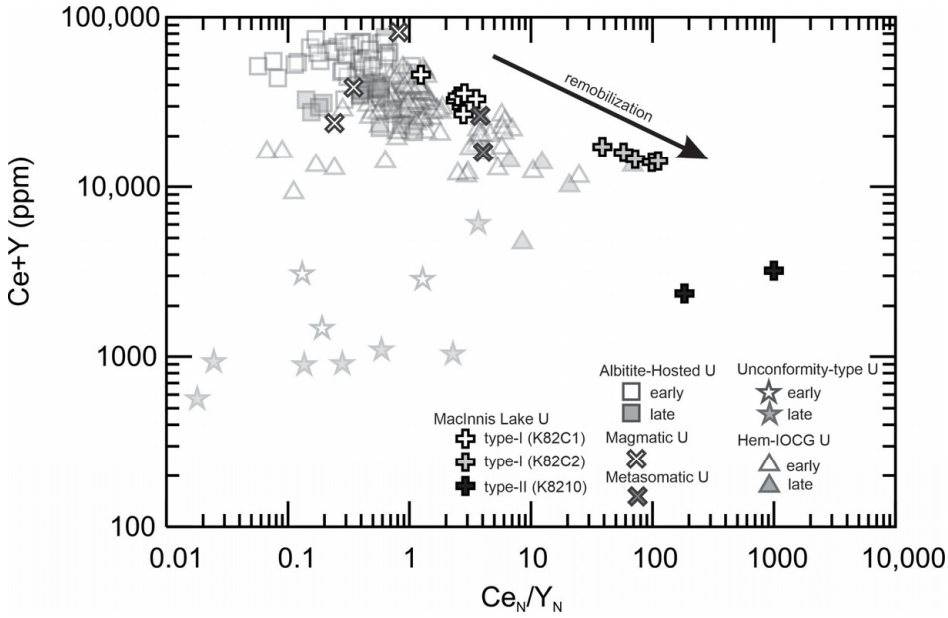


**Figure 12.** Chondrite-normalized $Ce_N/Y_N$ ratios vs. Ce+Y for uraninite from various deposit types compared to the MacInnis Lake uranium occurrences, including data from Potter et al. [65] and Mercadier et al. [20]. Normalization values from McDonough and Sun [44].

Uranium enrichment is common in regionally occurring metasomatic iron and alkali calcic (MIAC) systems that host various mineral deposits, most notably albitite-hosted uranium deposits and U-bearing IOCG [46,51,66–70]. These MIAC ore systems occur globally and exhibit high to low temperature alteration facies of distinct geochemical and mineralogical compositions, and which host discrete mineral deposit types (see detailed overview [68]). Important for this study are (i) Na-dominate albitites that may be barren, or overprinted by later fluids to form albitite-hosted uranium deposits, and (ii) K-Fe alteration zones consisting of high temperature (>350 °C) magnetite-type IOCG deposits with biotite and/or K-feldspar, and/or low temperature (250–350 °C;) hematite-group IOCG deposits with K-feldspar and/or sericite [46,66,70]. This is not the first study to compare Nonacho Basin mineral occurrences to deposits of MIAC systems. The Mosquito Gulch occurrence, located in the southeastern Nonacho Basin, has been proposed as an albitite-hosted uranium occurrence [71] (Figure 2a). More recent work also speculates on the potential for IOCG and affiliated deposits (polymetallic skarn, albitite-hosted uranium and epithermal deposits) at the Crest occurrence (Figure 2a) within the Nonacho Basin and in the adjacent East Arm region of Great Slave Lake (Figure 1) [18,51].

We note that the uranium occurrences at MacInnis Lake exhibit many similarities to albitite-hosted uranium deposits [48,72–75]. These deposits post-date extensive metasomatic albitization along regional deformation zones, and may occur with more local K-Fe alteration facies [48,51]. The alteration minerals that pre-date type-i uranium minerals of the Kult-82 occurrence (e.g., K-feldspar, magnetite, Cu-sulphides, Ti-oxides; Figures 3 and 4) are similar to mineral associations for primary uraninite in albitite-hosted uranium occurrences of the Southern Breccia, Great Bear Magmatic Zone [51], northwest of the Nonacho Basin area at the western margin of the Wopmay Orogen. Primary uraninite of the Southern Breccia occur with a high temperature facies of K-feldspar, biotite, magnetite, Ti-oxides and Cu-sulfides cross-cutting earlier albitization [51]. The mineral associations and texture of type-ii uranium minerals of Kult-82 are similar to secondary uranium minerals of the Southern Breccia occurring within breccias and veinlets with hematite, chlorite and K-feldspar. Compositionally, the high ΣREE and $LREE_N/HREE_N$ ratios of type-i and type-ii uranium minerals are also similar to primary and secondary uranium minerals of the Southern Breccia, respectively (Figure 12; [51]). However, both type-i and -ii uranium minerals of the

Kult-82 occurrence have low Th, consistent only with secondary uranium minerals of the Southern Breccia owing to the immobile nature of Th at low temperature.

Another notable metasomatic albitite-hosted deposit that shares considerable similarities in mineral paragenesis and uranium mineral chemistry is the Gunnar deposit of the Beaverlodge area of northern Saskatchewan, ~150 km southeast of the Nonacho Basin. The Beaverlodge district hosts numerous uranium deposits recording at least six stages of mineralization, with early 2.3 Ga basement mineralization that formed during retrogression of Arrowsmith Orogen to ~1.62 Ga late veins "Athabasca type" produced by the circulation of basinal fluids from the overlying Martin Lake Basin [76]. The Gunnar deposit formed between 2.3 to 1.85 Ga after the emplacement of the 2.32 Ga Gunnar granite host rock. Uranium mineralization formed predominately during two stages: (i) Na-metasomatism between 2.3 and 1.85 Ga, related to magmatic activity that produced uraninite with chlorite, calcite, hematite, titanite and monazite, and (ii) later breccia-type uraninite-brannerite with chlorite, calcite and hematite related to the early Trans Hudson Orogen at 1.85 Ga [76]. Both metasomatic and breccia-type uraninite formed at temperatures from 315 to 330 °C, are Th poor (<0.1 wt.% $ThO_2$), and have high REE (>1.5 wt.%) and $LREE_N/HREE_N$ ratios (~4.5), comparable to the Kult-82 occurrence uraninite-uranophane [76]. Considering the similarities between uranium mineralization of MacInnis Lake and the Gunnar deposit, could uranium mineralization of the Nonacho Basin also be multi-stage? For example, some basement occurrences where albitization and K-feldspar alteration is pervasive, such as Kult-82 and Island, may have initiated earlier in the MIAC system, providing sites for later uranium mineralization.

We also note many similarities between the uranium occurrences at MacInnis Lake and U-bearing low temperature K-Fe alteration facies and hematite group IOCG deposits of MIAC systems [46] that exhibit mineral assemblages of K-feldspar or sericite, ±calcite and chlorite, ±chalcopyrite, bornite, chalcocite, REE, or U-bearing minerals. Similarly, host rocks at MacInnis Lake have undergone extensive albitization, potassic alteration as Ba-rich K-feldspar and/or sericite that are locally associated with vein and breccia-hosted uranium mineralization. Similar to type-ii uranium minerals at MacInnis Lake, intense hematite and sericite breccias are associated with uranium mineralization at the Olympic Dam hematite group IOCG deposit of Australia [77]. The mineralized rocks at MacInnis Lake also contain elevated Cu, Ag, LREE, Bi, Ba and U (Table S2; Figure 11d–f), similar to metallic assemblage common in IOCG deposits in low-temperature K-Fe alteration facies [46,77], as seen at Olympic Dam [29]. The MacInnis Lake uranium minerals have similar compositions to uraninite from the Nori and Fab IOCG deposits of the Great Bear Magmatic Zone [51]. These deposits are associated with low-temperature K-Fe alteration [78], and host primary and secondary uraninite that contain elevated Si, Ca, Fe and Pb [65]. The ΣREE of Nori uraninite are consistent with type-i uranium minerals, while the $LREE_N/HREE_N$ ratios are more similar to that of type-ii uraninite-uranophane. Nori uraninite also exhibits low Th (<0.30 wt.% $ThO_2$); the result of low-temperature (<350 °C) hydrothermal processes. Overall, the MacInnis Lake uranium minerals have similar high ΣREE, $LREE_N/HREE_N$ ratios, mineral chemistry (e.g., elevated Si, Ca, low Th), mineral associations (e.g., chlorite, hematite, chalcopyrite) and temperature (<350 °C) to uranium mineralization associated with the low-temperature metasomatic K-Fe alteration facies of the Great Bear Magmatic Zone MIAC system.

In summary, type-i and type-ii uranium minerals at MacInnis Lake contain high ΣREE, $LREE_N/HREE_N$ ratios > 1, and are poor in Th. Their high REE concentrations are comparable to magmatic, syn-metamorphic and IOCG style uraninite mineralization; however, the low Th content (<0.12 wt.% $ThO_2$) occurrence with low-temperature (313–333 °C) chlorite is inconsistent with that of high-temperature MIAC affiliated deposits (e.g., magnetite group IOCG, albitite-hosted uranium) or other high-temperature (i.e., intrusive, metamorphic) mineralization. Instead, the low-temperature (<350 °C) hydrothermal uranium minerals and rocks at MacInnis Lake show chemical (i.e., enriched Cu, Ag, LREE, Bi, Ba and U) and mineralogical (i.e., hematite, K-feldspar, sericite, calcite, chlorite, chalcopyrite, bor-

nite, and U-minerals) similarities with the uraninite in low-temperature hematite group IOCG deposits of the K-Fe alteration facies in MIAC systems, as well as metasomatic and breccia-type uranium of the Gunnar deposit in the Beaverlodge district.

Metasomatic iron and alkali-calcic mineral systems typically occur within geological belts spanning hundreds of kilometers, where development of alteration facies depends on a variety of factors (e.g., depth and metasomatic pathway of fluids) [65–70]. The low-temperature K-Fe alteration associated with the uranium occurrences at MacInnis Lake, and the geological context of the Nonacho Basin as a structurally controlled, highly deformed and altered basin that underwent multiple tectono-metamorphic events [24,25,29,79] that is proximal to orogenic zones (i.e., Taltson and Thelon suture zones) suggests potential for hematite-group IOCG deposits and MIAC alteration systems in the area.

## 6. Conclusions

Uranium mineralization at MacInnis Lake is hosted in albitized and potassic altered sub-Nonacho basement granitoids and in overlying sedimentary units and gabbroic intrusions along structural corridors within the MacInnis Lake sub-basin. Two types of uranium minerals are characterized: type-i) uranophane ± uraninite, with or without galena, as overgrowths on earlier, partially dissolved bornite and chalcopyrite in quartz-chlorite ± calcite veins and stockwork (i.e., Kult-82 and Dussault), and type-ii) a chemically and paragenetically distinct phase of uranophane spatially associated with, or as micro-inclusions within, hematite and/or rutile in quartz and pervasively sericitized chlorite veins, stockwork and breccias (i.e., Kult-82, Island, Cole and Welch). Both types of uranium minerals at MacInnis Lake contain elevated ΣREE+Y and $LREE_N/HREE_N$ ratio $\geq 1$. There are many similarities between the uranium mineral chemistry (e.g., elevated ΣREE+Y, Si, Ca, low Th), mineral associations (i.e., hematite, K-feldspar, sericite, calcite, chlorite, chalcopyrite, bornite, and U-minerals), and whole rock geochemistry (Cu, Ag, LREE, Bi, Ba, U+/− Au) with mineral deposits characteristic of low-temperature K-Fe alteration facies of MIAC systems globally, such as hematite-type IOCG deposits (e.g., Olympic Dam in Australia, and the Nori and Fab IOCG deposits of the Great Bear Magmatic Zone, Canada),. The MacInnis Lake uranium occurrences are classified as metasomatic uranium formed from low-temperature (<350 °C) hydrothermal fluids associated with K-Fe alteration in an MIAC system, and suggest that there is a potential for MIAC affiliated mineral deposits in the area.

**Supplementary Materials:** The following supporting information can be downloaded at: https://www.mdpi.com/article/10.3390/min12121609/s1.

**Author Contributions:** Conceptualization, E.A., J.H., H.F. and E.M.; methodology, E.A.; formal analysis, K.L.; writing—original draft preparation, K.L.; writing—review and editing, E.A., H.F., J.H., A.R.-G. and A.T.; supervision, E.A.; project administration, H.F.; funding acquisition, E.M. All authors have read and agreed to the published version of the manuscript.

**Funding:** This research was funded by the Northwest Territories Geological Survey.

**Acknowledgments:** We thank Yanan Liu from the University of Toronto for EPMA work and Brandon Boucher from the University of New Brunswick for Micro-XRF work. We also acknowledge collaborators of the Nonacho Bedrock Mapping Project. Many thanks are extended to three anonymous reviewers and David Quirt, academic editor, for their insightful reviews that helped improve the manuscript.

**Conflicts of Interest:** The authors declare no conflict of interest.

## References

1. Meagher, J.T. *Report on the BAG Claim Group, MacInnis Lake, Northwest Territories*; Department of Indian and Northern Affairs Document No. N017070; ISO Uranium Mined Limited: Calgary, AB, Canada, 1955.
2. Reid, J.D. *MacInnis Lake: Report on Area for Exploration*; Unpublished Report; Scurry-Rainbow Oil Limited: Calgary, AB, Canada, 1955.
3. Checklin, G.A. *MacInnis Lake Project (AFE 2-27)*; Unpublished Report; Scurry-Rainbow Oil Limited: Calgary, AB, Canada, 1968.
4. Makela, K. *MacInnis Lake Property Evaluation*; Unpublished Report; Scurry-Rainbow Oil Limited: Calgary, AB, Canada, 1970.

5. Moffat, G.W. An Investigation of the Radioactive Mineral Occurrences of the Great Slake Lake-Athabasca Lake Region of the District of Mackenzie in the Northwest Territories. Unpublished Bachelor's Thesis, University of Toronto, Toronto, ON, Canada, 1974.
6. MacLeod, W.A.; Brander, J.M. *Assessment Report: Mining Claims BM 1-36, Claim Map No. 75E-8 (Lat. 61°20′; Long. 110°10′) August 1, 1974-October 1, 1974*; Department of Indian and Northern Affairs Document No. N 080170; Shell Canada Limited: Calgary, AB, Canada, 1975.
7. Gandhi, S.S.; Prasad, N. Geology and Uranium Occurrences of the Macinnis Lake Area, District of Mackenzie. In *Current Research Part B/Recherches en Cours Partie B*; Paper no. 80-1B; Geological Survey of Canada: Ottawa, ON, Canada, 1980; pp. 107–127. [CrossRef]
8. Harrington, E. *Thekuthili Lake Project, Northwest Territories, Assessment Work Report-1979*; Unpublished Report; PNC Exploration (Canada) Limited: Vancouver, BC, Canada, 1980.
9. Kuronuma, C. *Assessment Report of the Thekuthili Lake Project on Mineral Claims Kule 13, 41, 48, 51, 52, 53, 59, 71, 72, 74, 75, 76, 77, 78, 79, 80, 81, 82*; Geology Ontario: Toronto, ON, Canada, 1984.
10. Spencer, R. *MacInnis Group: Engineering Report No. 1 (Mine Series No. 5831)*; Unpublished Report; Consolidated Mining and Smelting Company of Canada Limited: Vancouver, BC, USA, 1955.
11. Campbell Todd, R. *Report on Exploration on the MacInnis Lake Property of Canadian Pipelines and Petroleum Limited, Northwest Ter-ritories*; Unpublished Report; Northwest Territories; Scurry-Rainbow Oil Limited: Calgary, AB, Canada, 1956.
12. McVittie, G.A. *Report on Packsack Drilling: Bragon Zone*; Unpublished Report; Consolidated Mining and Smelting Company of Canada Limited: Vancouver, BC, USA, 1956.
13. Stephen, H.C. *Geological Report on the WALT Claim Group, MacInnis Lake, Taltson Lake Map Area, District of Mackenzie, Northwest Territories*; Department of Indian and Northern Affairs, Document No. N017080; Newkirk Mining Corporation Limited: Toronto, ON, Canada, 1956.
14. MacDonald, B. *Report on Exploration on the MacInnis Lake Property of Canadian Pipelines and Petroleum Limited, Northwest Ter-ritories*; Unpublished Report; Scurry-Rainbow Oil Limited: Calgary, AB, Canada, 1956.
15. Koehler, G.J. *Geological Report, MacInnis Property, Island Zone; Mackenzie Mining District, N.W.T.*; Unpublished Report; Consolidated Mining and Smelting Company Limited: Vancouver, BC, USA, 1957.
16. Mellion, J.J. *Report on the Nonacho Project, Summer 1965*; Unpublished Report; International Mine Services Limited: Surrey, BC, Canada, 1965.
17. Hegge, M.R.; Trigg, C.M. *Results of Diamond Drilling on Claim No. 22, Pyramid Group, MacInnis Lake, Northwest Territories*; Department of Indian and Northern Affairs Document No. N019973; Territorial Uranium Miners Limited: Ottawa, ON, Canada, 1967.
18. Jefferson, C.W. Uranium Potential and Levels of Radioactivity in the Proposed National Park Area. In *Mineral and Energy Resource Assessment of the Proposed Thaidene Nene National Park Reserve in the Area of the East Arm of Great Slave Lake, Northwest Territories*; Open File 7196; Wright, D.F., Ambrose, E.J., Lemkow, D., Bonham-Carter, G., Eds.; Geological Survey of Canada: Ottawa, ON, Canada, 2013; pp. 363–375. [CrossRef]
19. Finch, R.; Murakami, T. Systematics and Paragenesis of Uranium Minerals. *Uranium* **1999**, *38*, 91–180. [CrossRef]
20. Mercadier, J.; Cuney, M.; Lach, P.; Boiron, M.-C.; Bonhoure, J.; Richard, A.; Leisen, M.; Kister, P. Origin of uranium deposits revealed by their rare earth element signature. *Terra Nova* **2011**, *23*, 264–269. [CrossRef]
21. Alexandre, P.; Kyser, K.; Layton-Matthews, D.; Joy, B.; Uvarova, Y. Chemical Compositions of Natural Uraninite. *Can. Miner.* **2015**, *53*, 595–622. [CrossRef]
22. Alexandre, P.; Kyser, T.K. Effects of cationic substitutions and alteration in uraninite, and implications for the dating of uranium deposits. *Can. Miner.* **2005**, *43*, 1005–1017. [CrossRef]
23. Kotzer, T.G.; Kyser, T.K. O, U, and Pb Isotopic and Chemical Variations in Uraninite: Implications for Determining the Tem-poral and Fluid History of Ancient Terrains. *Am. Mineral.* **1993**, *78*, 1262–1274.
24. Pehrsson, S.J.; Berman, R.G.; Eglington, B.; Rainbird, R. Two Neoarchean supercontinents revisited: The case for a Rae family of cratons. *Precambrian Res.* **2013**, *232*, 27–43. [CrossRef]
25. Hoffman, P.F. United Plates of America, the Birth of a Craton: Early Proterozoic Assembly and Growth of Laurentia. *Annu. Rev. Earth Planet. Sci.* **1988**, *16*, 543–603. [CrossRef]
26. Pehrsson, S.; Berman, R.; Davis, W. Paleoproterozoic orogenesis during Nuna aggregation: A case study of reworking of the Rae craton, Woodburn Lake, Nunavut. *Precambrian Res.* **2013**, *232*, 167–188. [CrossRef]
27. Berman, R.G.; Davis, W.J.; Sanborn-Barrie, M.; Whalen, J.B.; Taylor, B.E.; McMartin, I.; McCurdy, M.W.; Mitchell, R.K.; Ma, S.; Coyle, M.; et al. *Report of activities for the GEM-2 Chantrey-Thelon activity: Thelon Tectonic Zone project, Nunavut*; Geological Survey of Canada: Ottawa, ON, Canada, 2018. [CrossRef]
28. Aspler, L.B.; Donaldson, J.A. *The Nonacho Basin (Early Proterozoic), Northwest Territories, Canada: Sedimentation and Deformation in a Strike-Slip Setting*; Strike-Slip Deformation, Basin Formation, and Sedimentation (SP37); Natural Resources Canada: Ottawa, ON, Canada, 1985; pp. 193–209. [CrossRef]
29. Ashton, K.; Hartlaub, R.; Heaman, L.; Morelli, R.; Card, C.; Bethune, K.; Hunter, R. Post-Taltson sedimentary and intrusive history of the southern Rae Province along the northern margin of the Athabasca Basin, Western Canadian Shield. *Precambrian Res.* **2009**, *175*, 16–34. [CrossRef]

30. van Breemen, O.; Kjarsgaard, B.A.; Tella, S.; Lemkow, D.; Aspler, L. U-Pb Detrital Zircon Geochronology of Clastic Sedimentary Rocks of the Paleoproterozoic Nonacho and East Arm Basins, Thaidene Nena MERA Study Area. In *Mineral and Energy Resource Assessment of the Proposed Thaidene Nene National Park Reserve in the Area of the East Arm of Great Slave Lake, Northwest Territories*; Wright, D.F., Ambrose, E.J., Lemkow, D., Bonham-Carter, G., Eds.; Geological Survey of Canada: Ottawa, ON, Canada, 2013; Volume 119142. [CrossRef]
31. Neil, B.J.; Gibson, H.D.; Pehrsson, S.J.; Martel, E.; Thiessen, E.J.; Crowley, J.L. Provenance, stratigraphic and precise depositional age constraints for an outlier of the 1.9 to 1.8 Ga Nonacho Group, Rae craton, Northwest Territories, Canada. *Precambrian Res.* **2020**, *352*, 105999. [CrossRef]
32. Ielpi, A.; Martel, E.; Fischer, B.; Pehrsson, S.J.; Tullio, M.; Neil, B.J. A reappraisal of the Nonacho Basin (Northwest Territories, Canada): Record of post-orogenic collapse and marine flooding in the Palaeoproterozoic of the Rae Craton. *Precambrian Res.* **2021**, *358*, 106140. [CrossRef]
33. Aspler, L.B. Geology of Nonacho Basin (Early Proterozoic) N.W.T. Ph.D. Thesis, Carleton University, Ottawa, ON, Canada, 1985.
34. Henderson, J.F. *Nonacho Lake Area, Northwest Territories*; Paper 37-2; Geological Survey of Canada: Ottawa, ON, Canada, 1937; p. 22.
35. Bostock, H.H.; van Breemen, O. *The timing Of emplacement, and Distribution of the Sparrow Diabase Dyke Swarm, District of Mackenzie, Northwest Territories*; Radiogenic Age and Isotopic Studies: Report 6, Paper 92-2; Geological Survey of Canada: Ottawa, ON, Canada, 1992; ISBN 0660147564.
36. Canam, R.; Gibson, H.d.; Martel, E.; Kellet, D. The Timing of Deformation and Kinematics of Shear Zones in the Nonacho Lake Area. In Proceedings of the Yellowknife Geoscience Forum: Geoscience and Exploration, Online, 24–26 November 2021.
37. Maurice, Y.T. *Gold, Tin, Uranium and Other Elements in the Proterozoic Nonacho Sediments and Adjacent Basement Rocks near MacInnis Lake, District of Mackenzie*; Paper 84-1A; Geological Survey of Canada: Ottawa, ON, Canada, 1984; pp. 229–238.
38. NORMIN. NORMIN Showings [Online]. Available online: http://www.ntgomap.nwtgeoscience.ca (accessed on 24 July 2019).
39. Bowles, J.F. Age Dating from Electron Microprobe Analyses of U, Th, and Pb: Geological Advantages and Analytical Difficulties. *Microsc. Microanal.* **2015**, *21*, 1114–1122. [CrossRef] [PubMed]
40. Bowles, J.F. Age dating of individual grains of uraninite in rocks from electron microprobe analyses. *Chem. Geol.* **1990**, *83*, 47–53. [CrossRef]
41. Wiewióra, A. Crystallochemical classifications of phyllosilicates based on the unified system of projection of chemical composition: III. The serpentine-kaolin group. *Clay Miner.* **1990**, *25*, 93–98. [CrossRef]
42. Bourdelle, F.; Cathelineau, M. Low-temperature chlorite geothermometry: A graphical representation based on a T–R2+ –Si diagram. *Eur. J. Miner.* **2015**, *27*, 617–626. [CrossRef]
43. Alexandre, P.; Uvarova, Y.; Kyser, T.K. Origin of Uranous and Uranyl Minerals at the Centennial Deposit, Athabasca Basin, Northern Saskatchewan, Canada. *Can. Miner.* **2012**, *50*, 693–704. [CrossRef]
44. McDonough, W.F.; Sun, S.-S. The composition of the Earth. *Chem. Geol.* **1995**, *120*, 223–253. [CrossRef]
45. Hövelmann, J.; Putnis, A.; Geisler, T.; Schmidt, B.C.; Golla-Schindler, U. The replacement of plagioclase feldspars by albite: Observations from hydrothermal experiments. *Contrib. Miner. Pet.* **2009**, *159*, 43–59. [CrossRef]
46. Corriveau, L.; Montreuil, J.-F.; Potter, E. Alteration Facies Linkages Among Iron Oxide Copper-Gold, Iron Oxide-Apatite, and Affiliated Deposits in the Great Bear Magmatic Zone, Northwest Territories, Canada. *Econ. Geol.* **2016**, *111*, 2045–2072. [CrossRef]
47. Putnis, A.; Hinrichs, R.; Putnis, C.V.; Golla-Schindler, U.; Collins, L.G. Hematite in porous red-clouded feldspars: Evidence of large-scale crustal fluid–rock interaction. *Lithos* **2007**, *95*, 10–18. [CrossRef]
48. Wilde, A. Towards a Model for Albitite-Type Uranium. *Minerals* **2013**, *3*, 36–48. [CrossRef]
49. Janeczek, J.; Ewing, R. Dissolution and alteration of uraninite under reducing conditions. *J. Nucl. Mater.* **1992**, *190*, 157–173. [CrossRef]
50. Ono, S.; Fayek, M. Decoupling of O and Pb isotope systems of uraninite in the early Proterozoic Conglomerates in the Elliot Lake district. *Chem. Geol.* **2011**, *288*, 1–13. [CrossRef]
51. Potter, E.; Montreuil, J.; Corriveau, L.; Davis, W. The Southern Breccia Metasomatic Uranium System of the Great Bear Magmatic Zone, Canada. *Ore Depos. Orig. Explor. Exploit.* **2019**, 109–130. [CrossRef]
52. Cuney, M. The extreme diversity of uranium deposits. *Miner. Depos.* **2008**, *44*, 3–9. [CrossRef]
53. Yeo, G.M.; Potter, E.G. Review of Reducing Mechanisms Potentially Involved in the Formation of Unconformity-Type Uranium Deposits and Their Relevance to Exploration. *Sask. Geol. Surv.* **2010**, *2*, 13.
54. Richard, A.; Rozsypal, C.; Mercadier, J.; Banks, D.A.; Cuney, M.; Boiron, M.-C.; Cathelineau, M. Giant uranium deposits formed from exceptionally uranium-rich acidic brines. *Nat. Geosci.* **2011**, *5*, 142–146. [CrossRef]
55. Richard, A.; Banks, D.A.; Mercadier, J.; Boiron, M.-C.; Cuney, M.; Cathelineau, M. An evaporated seawater origin for the ore-forming brines in unconformity-related uranium deposits (Athabasca Basin, Canada): Cl/Br and δ37Cl analysis of fluid inclusions. *Geochim. Cosmochim. Acta* **2011**, *75*, 2792–2810. [CrossRef]
56. Pagel, M.; Poty, B.; Sheppard, S.M.F. *Contributions to Some Saskatchewan Uranium Deposits Mainly from Fluid Inclusions and Isotopic Data*; Ferguson, S., Gobely, A., Eds.; Uranium Pine Creek Geosyncline: Vienna, Austria, 1980; pp. 639–654.
57. Kotzer, T.; Kyser, T. Petrogenesis of the Proterozoic Athabasca Basin, northern Saskatchewan, Canada, and its relation to diagenesis, hydrothermal uranium mineralization and paleohydrogeology. *Chem. Geol.* **1995**, *120*, 45–89. [CrossRef]

58. Jefferson, C.W.; Thomas, D.J.; Gandhi, S.S.; Ramaekers, P.; Delaney, G.; Brisbin, D.; Cutts, C.; Portella, P.; Olson, R.A. Unconformity-Associated Uranium Deposits of the Athabasca Basin, Saskatchewan and Alberta. *Bull. Geol. Surv. Canada* **2007**, *588*, 23–67. [CrossRef]
59. Adlakha, E.E.; Hattori, K. Paragenesis and Composition of Tourmaline Types Along the P2 Fault and Mcarthur River Uranium Deposit, Athabasca Basin, Canada. *Can. Miner.* **2016**, *54*, 661–679. [CrossRef]
60. Alexandre, P.; Kyser, K.; Polito, P.; Thomas, D. Alteration Mineralogy and Stable Isotope Geochemistry of Paleoproterozoic Basement-Hosted Unconformity-Type Uranium Deposits in the Athabasca Basin, Canada. *Econ. Geol.* **2005**, *100*, 1547–1563. [CrossRef]
61. Fayek, M.; Kyser, T.K. Characterization of Multiple Fluid-Flow Events and Rare-Earth-Element Mobility Associated with Formation of Unconformity-Type Uranium Deposits in the Athabasca Basin, Saskatchewan. *Can. Mineral.* **1997**, *35*, 627–658.
62. Alexandre, P.; Kyser, K.; Thomas, D.; Polito, P.; Marlat, J. Geochronology of unconformity-related uranium deposits in the Athabasca Basin, Saskatchewan, Canada and their integration in the evolution of the basin. *Miner. Depos.* **2007**, *44*, 41–59. [CrossRef]
63. Ng, R.; Alexandre, P.; Kyser, K.; Cloutier, J.; Abdu, Y.A.; Hawthorne, F.C. Oxidation state of iron in alteration minerals associated with sandstone-hosted unconformity-related uranium deposits and apparently barren alteration systems in the Athabasca Basin, Canada: Implications for exploration. *J. Geochem. Explor.* **2013**, *130*, 22–43. [CrossRef]
64. Mcglynn, J.C.; Irving, E.; Park, J.K. Paleomagnetism and Age of Nonacho Group Sandstone and Associated Sparrow Dikes, District of Mackenzie. *Can. J. Earth Sci.* **1974**, *11*, 30–42. [CrossRef]
65. Potter, E.G.; Corriveau, L.; Montreuil, J.; Yang, Z.; Potter, E.G.; Corriveau, L.; Montreuil, J. *Uranium Enrichment Processes in Metasomatic Iron Oxide and Alkali-Calcic Systems as Revealed by Uraninite Trace Element Chemistry—Supplementary Data*; Open File 8798; Geological Survey of Canada: Ottawa, ON, Canada, 2021.
66. Potter, E.; Corriveau, L.; Kjarsgaard, B. Paleoproterozoic Iron Oxide Apatite (IOA) and Iron Oxide-Copper-Gold (IOCG) mineralization in the East Arm Basin, Northwest Territories, Canada. *Can. J. Earth Sci.* **2020**, *57*, 167–183. [CrossRef]
67. Corriveau, L.; Montreuil, J.-F.; De Toni, A.F.; Potter, E.G.; Percival, J.B. Mapping mineral systems with IOCG and affiliated deposits: A facies approach. In *Mineral Systems with Iron Oxide Copper-Gold (IOCG) and Affiliated Depos*; Special Paper 52; Corriveau, L., Potter, E.G., Mumin, A.H., Eds.; Geological Association of Canada: Ottawa, ON, Canada, 2022; pp. 69–111.
68. Corriveau, L.; Mumin, A.H.; Potter, E.G. Introduction and overview. In *Mineral Systems with Iron Oxide Copper-Gold (IOCG) and Affiliated Deposits*; Corriveau, L., Potter, E.G., Mumin, A.H., Eds.; Special Paper 52; Geological Association of Canada: Ottawa, ON, Canada, 2022; pp. 1–26.
69. Skirrow, R.G. Hematite-group IOCG ± U deposits: An update on their tectonic settings, hydrothermal characteristics, and Cu-Au-U mineralizing processes. In *Mineral Systems with Iron Oxide-Copper-Gold (IOCG) and Affiliated Deposits*; Special Paper 52; Corriveau, L., Potter, E.G., Mumin, A.H., Eds.; Geological Association of Canada: Ottawa, ON, Canada, 2022; pp. 27–51.
70. Corriveau, L.; Montreuil, J.-F.; Blein, O.; Ehrig, K.; Potter, E.G.; Fabris, A.; Clark, J. *Mineral systems with IOCG and affiliated deposits: Part 2—Geochemical footprints. In Mineral Systems with Iron Oxide-Copper-Gold (IOCG) and Affiliated Deposits*; Special Paper 52; Corriveau, L., Potter, E.G., Mumin, A.H., Eds.; Geological Association of Canada: Ottawa, ON, Canada, 2022; pp. 159–204.
71. Gatzweiler, R.; Von Pechmann, E.; Loewer, R.; Strnad, G.; Fritsche, R. *Albitite-Type Uranium Mineralization in the Nonacho Basin Area, Northwest Territories, Canada*; International Atomic Energy Agency (IAEA): Vienna, Austria, 1987; pp. 491–518.
72. Belevtsev, Y. Endogenic uranium deposits of precambrian shields: Environment of deposition. In *Albitized Uranium Deposits: Six Articles Translated from Russian Literature*; United States Department of Energy: Washington, DC, USA, 1980; pp. 55–80.
73. Grechishnicov, N. Structural setting of one type of uranium-albitite mineralisation in Precambrian rocks. In *Albitized Uranium Deposits: Six Articles Translated from Russian Literature*; United States Department of Energy: Washington, DC, USA, 1980.
74. Cinelu, S.; Cuney, M. Sodic metasomatism and U–Zr mineralization: A model based on the Kurupung batholith (Guyana). *Geochim. Cosmochim. Acta* **2006**, *70*, A103. [CrossRef]
75. Alexandre, P. Mineralogy and geochemistry of the sodium metasomatism-related uranium occurrence of Aricheng South, Guyana. *Miner. Depos.* **2010**, *45*, 351–367. [CrossRef]
76. Dieng, S.; Kyser, K.; Godin, L. Genesis of Multifarious Uranium Mineralization in the Beaverlodge Area, Northern Saskatchewan, Canada. *Econ. Geol.* **2015**, *110*, 209–240. [CrossRef]
77. Ehrig, K.; McPhie, J.; Kamenetsky, V. Geology and Mineralogical Zonation of the Olympic Dam Iron Oxide Cu-U-Au-Ag Deposit, South Australia. In *Geology and Genesis of Major Copper Deposits and Districts of the World: A Tribute to Richard H. Sillitoe, Jeffrey W. Hedenquist, Michael Harris, Francisco Camus*; Society of Economic Geologists: Littleton, CO, USA, 2012.
78. Ootes, L.; Goff, S.; Jackson, V.A.; Gleeson, S.A.; Creaser, R.A.; Samson, I.M.; Evensen, N.; Corriveau, L.; Mumin, A.H. Timing and thermochemical constraints on multi-element mineralisation at the Nori/RA Cu–Mo–U prospect, Great Bear magmatic zone, Northwest Territories, Canada. *Miner. Depos.* **2010**, *45*, 549–566. [CrossRef]
79. Berman, R.G. *Metamorphic Map of the Western Churchill Province*; Open File 5279 (3 Sheets 49 P. Rep.); Geological Survey of Canada: Ottawa, ON, Canada, 2010.